

**Evidence for decadal variability
in an ocean general circulation model:
An advective mechanism**

Andrew J. Weaver and E.S. Sarachik

C²GCR Report No. 90-9

July 1990

Evidence for decadal variability in an ocean general circulation model: An advective mechanism¹

Andrew J. Weaver²

Department of Meteorology
McGill University
805 Sherbrooke St. West
Montreal, P.Q., H3A 2K6
Canada

and

E. S. Sarachik

Joint Institute for the Study of the Atmosphere and Ocean
University of Washington, AK-40
Seattle, Washington, 98195

Submitted to
Atmosphere-Ocean
R.W Stewart Symposium Edition
July, 1990

¹ JISAO Contribution No. #112

² Also Centre for Climate and Global Change Research, McGill University

Abstract

A series of numerical experiments involving long-time integrations are conducted using the Bryan-Cox Ocean General Circulation Model under mixed surface boundary conditions (i.e., a Newtonian restoring surface boundary condition on temperature and a specified flux boundary condition on salinity). Under steady forcing the system oscillates with significant energy at decadal period. This oscillation is shown to be an advective phenomenon, associated with the propagation of salinity and temperature anomalies from the region between the subtropical and subpolar gyres, where they are generated, to the eastern boundary, where deep water is formed. Furthermore, the oscillation involves the turning on and shutting off of deep water formation. The poleward heat transport drops by nearly a factor of three between the stages of the oscillation when deep water is being formed and when the thermohaline circulation is collapsed. The observed decadal variability is robust in that it is present in all numerical experiments (12 and 33 vertical level models; one and two hemisphere models; synchronous and asynchronous integrations). Crucial to the existence of the variability is the use of a low vertical eddy viscosity coefficient.

1. Introduction

In attempting to explain the observed oceanic variability it is common to seek variability in its external forcing (e.g., solar heating, winds, evaporation/precipitation, attractive force of heavenly bodies, ice formation). Oceanic variability can be broken down into two components: That which is due to the variability in the external forcing and that which is due to internal variability within the system (e.g., baroclinic instability and eddy generation in a western boundary current). The relative importance of each is not always well understood. In this paper we consider several non-eddy resolving experiments in which we apply only steady forcing. As our surface thermal boundary condition we use a Haney (1971) formulation with a constant (in time) apparent atmospheric temperature. The heat flux into the ocean therefore varies with time as the model's surface temperatures vary, but the values to which these temperatures are restored do not vary. We show that there is significant decadal variability internal to the system and that this variability is linked fundamentally to high latitude convection and subsequent deep water formation.

There has been a good deal of scientific, economic and even political interest in changes in our global climate and their possible influences on our environment. This interest, together with the advent of a new generation of supercomputers, has lead many researchers to conduct coupled ocean-atmosphere simulations to study, for example, possible effects of a doubling of atmospheric CO₂ (e.g., Washington and Meehl, 1989; Stouffer *et al.*, 1989; Manabe *et al.*, 1990). Accurate continuous monitoring of atmospheric and oceanic variables has only existed since, at best, the turn of the century and in most cases since only after World War II. It is therefore very important to try and understand what ultra-low frequency variability exists in the ocean and indeed in the ocean general circulation models (OGCMs) used to model it, in order that we properly understand whether the changes we are observing in our environment and in our models are due to increasing greenhouse gases (for example) or indeed are simply part of a natural ultra-low frequency variability within the coupled ocean-atmosphere system.

There has recently been a lot of interest in possible decadal variability of the North Atlantic spawned by the observation of Dickson *et al.* (1988) of a *Great Salinity Anomaly* which was a widespread freshening of the upper layer of the subpolar gyre waters during 1968–1982. This feature was described by them as an advective event which could be traced around the subpolar gyre. The relationship between this salinity anomaly and the North Atlantic air-ice-ocean system is also receiving a lot of attention (e.g. Mysak and Manak, 1989; Ikeda, 1990; Mysak *et al.*, 1990). One of the reasons for such interest in the observations of the Great Salinity Anomaly in the North Atlantic is its links to the shutting

off and turning on of deep water formation (Lazier, 1980). Changes in deep water formation in turn affect the thermohaline circulation and the transport of heat from equatorial to polar regions. This poleward heat transport is one of the most important roles of the ocean in the earth's climatic system. The box model experiments which we conduct in this paper use forcing parameters typical of the region of the North Atlantic, however, neither an ice model nor an atmospheric model are coupled to the OGCM used herein.

In most numerical ocean modelling studies researchers use restoring boundary conditions on both surface temperature and salinity (or at least spin-up there model under such boundary conditions). These boundary conditions imply a direct feedback between oceanic surface values and atmospheric forcing variables, as discussed above for temperature. While there is a good deal of evidence justifying the use of the linear restoring boundary condition on the temperature field (e.g., Haney, 1971), there is less physical justification for the use of this condition on salinity. The appropriate boundary condition for salinity is a flux boundary condition i.e., specifying net fresh water input (precipitation – evaporation). We have chosen to use the latter boundary condition herein since none of the phenomena which we will discuss exist in a model that employs a restoring boundary condition on salinity. Weaver and Sarachik (1990b) discuss the implications of using restoring and mixed boundary conditions in OGCMs in more detail while Welander (1986) gives a fine review of phenomena related to the use of mixed boundary conditions.

As discussed by Weaver and Sarachik (1990a), general ocean circulation models must either use very large values for the vertical momentum diffusivity coefficient or very high vertical resolution to suppress computational modes which would otherwise be prevalent in the system. We will show that large values of this momentum diffusivity coefficient tend to suppress the variability within the system.

The outline of this paper is as follows: In Section 2 we describe numerical model while in Section 3 we introduce and discuss four numerical experiments which illustrate the decadal variability. In Section 4 we closely examine one particular oscillation and study its three-dimensional aspects. The sensitivity of our results to the vertical eddy viscosity coefficient is discussed in Section 5. We conclude with a brief summary in Section 6.

2. Description of the Numerical Model

The ocean general circulation model (OGCM) used in this study is the Cox (1984) version of the Bryan-Cox OGCM which is based on the primitive equation model described by Bryan (1979) and Bryan and Lewis (1979). The finite difference formulation of the governing equations is discussed in detail by Bryan (1969) and Cox (1984), while the polynomial approximation to the equation of state employed by the model is described by Bryan and Cox (1972). The model equations make use of the hydrostatic approximation, the Boussinesq approximation, the rigid-lid approximation and a turbulent closure scheme in which subgrid scale processes are modelled as enhanced mixing (lateral and vertical friction and diffusion). We use a 2° by 2° horizontal grid spacing with a 5000 m deep, flat-bottomed basin. The model domain in all experiments except Experiments 3 consists of a 60° wide southern hemisphere basin extending from 70° S to the equator. In Experiment 3 we extend the model domain to be from 70° S to 70° N. Table 1 summarizes the four experiments.

No-slip and insulating boundary conditions are applied at the lateral walls while at the equator a symmetric boundary condition is used. In Experiment 3 we remove this symmetry condition at the equator and at the new northern boundary (70° N) we once more apply no-slip and insulating conditions. The bottom is assumed to be impermeable and insulating. Bottom friction, which is assumed to be quadratic in velocity with a 10° turning angle (Gill, 1982) is also added. The wind stress which we choose to use can be represented by the simple analytic expression (F. Bryan, 1987 — Fig. 1a)

$$\tau^\lambda(\phi) = 0.2 + 0.8 \sin(6\phi) - \frac{1}{2}(1 + \tanh(10\phi)) - \frac{1}{2}(1 - \tanh(10(\frac{\pi}{2} + \phi))) \text{ dynes/cm}^2. \quad (1)$$

Here λ is the longitude and ϕ is the latitude in radians. There is only a zonal component to the wind stress (1) and furthermore the zonal component is only a function of latitude. Nevertheless, it captures the major features of the observed zonally averaged zonal wind stress (Fig. 1a). The surface boundary condition on temperature is a Newtonian restoring condition with a relaxation constant of 25 days (F. Bryan, 1987), i.e., the temperature at the first level of the model is relaxed to a zonally uniform reference temperature. This reference temperature (Fig. 1b) was obtained by averaging Levitus (1982) world ocean sea surface data over both the northern and southern hemispheres. A fixed flux boundary condition was specified on salinity. We used a surface salinity flux that was obtained from the steady state calculated by Weaver and Sarachik (1990a) in their 33 level run (Table 2 for the grid spacing), after 6133 surface (18398 bottom) years of integration with a Newtonian, restoring salinity surface boundary condition. The reference salinity which they used was also obtained by averaging Levitus (1982) world ocean sea surface data over both the

northern and southern hemispheres (Fig. 1c), while all of their other boundary conditions, as well as their model geometry, were identical to those used in the single hemisphere experiments (Experiments 1, 2, 4 and 5) discussed above. The salinity flux (Fig. 2) was diagnosed from their model by averaging the surface flux over 52 years of further integration. The basinwide mean salinity of the model of Weaver and Sarachik (1990a) was then calculated (33.697 ppt) and used as the initial salinity of a homogeneous rest state of constant temperature 5°C (Experiment 1). In the two basin experiment, Experiment 3, the initial condition was precisely that obtained by Weaver and Sarachik (1990a), reflected across the equator.

Vertical eddy viscosities and diffusivities were as used by Weaver and Sarachik (1990a,b) with the vertical eddy viscosity being everywhere set to $1.0 \text{ cm}^2\text{s}^{-1}$ and the vertical diffusivity being allowed to increase with depth from $A_{TVS}=0.3$ to $A_{TVB}=1.3 \text{ cm}^2\text{s}^{-1}$ according to the formula

$$A_{TV} = (A_{TV2500} + \frac{C_r}{\pi} \tan^{-1}[4.5 \times 10^{-3} \times (z - 2.5 \times 10^3)]) \text{ cm}^2\text{s}^{-1}. \quad (2)$$

Here $A_{TV2500}=0.8 \text{ cm}^2\text{s}^{-1}$ is the vertical diffusivity at a depth of 2500m and the range between the top and the bottom is given by $C_r=1.0 \text{ cm}^2\text{s}^{-1}$. As in Weaver and Sarachik (1990a,b), the horizontal eddy viscosity and diffusivity were set to $5 \times 10^8 \text{ cm}^2\text{s}^{-1}$ and $1 \times 10^7 \text{ cm}^2\text{s}^{-1}$, respectively, over the whole domain. In Section 5 we conduct an experiment in which we increase the vertical viscosity coefficient to $A_{MV} = 20 \text{ cm}^2\text{s}^{-1}$. A parameterization which allows lateral diffusion to occur along isopycnal surfaces (Cox, 1987) was not included although the parameterization which integrates convection into the diffusion process (Cox, 1984) was. In this latter parameterization, vertical diffusion was computed implicitly. When the water column became statically unstable the coefficient of vertical diffusivity was assigned a value of $10^4 \text{ cm}^2\text{s}^{-1}$.

In our initial three experiments, in which we were seeking stable equilibria of the highly nonlinear system as well as in Experiment 5, we sped up the convergence by using the acceleration techniques (asynchronous integration) of Bryan (1984). The barotropic vorticity and baroclinic velocity equations were integrated with a timestep of 1800 seconds which was different from that used in integrating the tracer equations for temperature and salinity (from 1 to 4 days, see Section 3). Furthermore, the tracer equation timestep was allowed to vary exponentially with depth (Bryan, 1984). At the deepest level the tracer equation timestep was three times its value at the surface level. Since one must exercise caution when discussing timescales associated with asynchronous integration we conduct an additional experiment, Experiment 4, in which we use synchronous integration (18000 seconds for all variables at all depths) through a 137 year period of decadal variability.

The depths of each level used in the 12 and 33 level experiments outlined in Table 1 and discussed in more detail in the next section, are given in Table 2.

3. The Numerical Experiments

In this section we describe the four numerical experiments in which the decadal oscillations were observed. The details and motivation behind these four experiments have been discussed in more detail by Weaver and Sarachik (1990b). What we will show is that under steady forcing there is a natural period of variability (decadal) within the fully nonlinear OGCM. The variability will be shown in Section 4 to be a high latitude phenomena linked inherently to the convection process. It is very relevant to point out that in a fully nonlinear, primitive equation atmospheric GCM, James and James (1989) also observed strong internal variability at the decadal timescale although different physical processes were involved.

3.1 Experiment 1

In the first experiment we take the salinity flux (Fig. 2) diagnosed from the 33 level steady state of Weaver and Sarachik (1990a), obtained after a total of 6133 surface (18398 bottom) years of integration, and spin up a 12 level model for 10760 surface years. We use a 2 day timestep for the first 110 surface years and a 1 day surface tracer timestep for all subsequent time. Figure 3 illustrates the kinetic energy density of this experiment throughout the run. As discussed by Weaver and Sarachik (1990b) the integration is characterized by quiescent periods of relatively little variability, periods of near decadal oscillations (Fig. 4a) and violent overturning flushes. The periods of decadal variability are shown as rapid oscillations of the kinetic energy density with amplitude of about $0.01 \text{ kgm}^{-1}\text{s}^{-2}$. What is evident from Fig. 4a is that the decadal oscillations are a persistent, periodic and uniform phenomena which occur through hundreds of years of integration, even under steady forcing. Over the 370 surface year period of decadal variability shown in Fig. 4a the system underwent 44 complete oscillations for a period of 8.4 surface years. Strictly speaking, we should not discuss timescales through an asynchronous integration, however, we will show in *Experiment 4*, that the period of oscillation only changes slightly upon switching to synchronous integration (i.e. same timestep for all variables at all depths). This follows since the oscillation is mainly a surface phenomena.

The meridional overturning streamfunction, which is generally thought of as a manifestation of the thermohaline circulation, is defined as follows: Consider the continuity equation in spherical coordinates,

$$u_{\lambda} + (v \cos\phi)_{\phi} + a \cos\phi w_z = 0 \quad , \quad (3)$$

where λ is longitude, ϕ is latitude and a is the radius of the Earth. The zonal integration of (3) from the western boundary λ_w to the eastern boundary λ_e gives,

$$\int_{\lambda_w}^{\lambda_e} (v \cos\phi)_{\phi} d\lambda + a \cos\phi \int_{\lambda_w}^{\lambda_e} w_z d\lambda = 0 , \quad (4)$$

since $u=0$ at $\lambda=\lambda_w$ and $\lambda=\lambda_e$. As (4) is non-divergent we may therefore define the meridional overturning streamfunction Φ by

$$-\Phi_z = \int_{\lambda_w}^{\lambda_e} v a \cos\phi d\lambda , \quad (5)$$

$$\frac{1}{a} \Phi_{\phi} = \int_{\lambda_w}^{\lambda_e} w a \cos\phi d\lambda , \quad (6)$$

assuming a basin of constant longitudinal width. Figures 4b, c and d illustrate the meridional overturning streamfunction at the three characteristic stages of the decadal oscillations portrayed in Fig. 4a. The oscillation is characterized by deep water formation (Fig. 4d — high kinetic energy, Fig. 4a) suddenly shutting off (Fig. 4c — lowering kinetic energy, Fig. 4a) followed by a reverse cell developing (lowest kinetic energy, Fig. 4a), intensifying slightly with time (Fig. 4b — increasing kinetic energy, Fig. 4a). The region of deep water formation then moves poleward until the structure portrayed in Fig. 4d is once more reached. The whole process repeats itself. At the equator unusual cells are present. These are generated by spurious convection associated with artificial sources and sink of tracer variables (from vertical Peclet number criterion violations, Weaver and Sarachik, 1990a).

3.2 Experiment 2

In order to show that these oscillations are not a consequence of the low vertical resolution we initialized a 33 level model with an intermediate state from the 12 level integration after 5804 surface (17413 bottom) years. The 12 level solution was interpolated onto the 33 level grid just before the flush (Fig. 3) with no modifications to the surface boundary conditions. The basin was then integrated forward for 3888 surface (11664 bottom) years. Figure 5 shows the corresponding kinetic energy density for this run. Upon switching to higher vertical resolution the system underwent the same flush as in the 12 level solution but this flush occurred almost immediately. After the flush, the system once more went into decadal oscillations after a long quiescent period. The oscillations are of the

same period and same structure as those discussed in Section 3.1 using only 12 vertical levels. In Section 3.4 we integrate through these oscillations with a synchronous timestepping procedure. Eventually these oscillations diminished and the basin evolved into a statistically steady state.

3.3 Experiment 3

In Experiment 3 we start off with the steady state 33 level model of Weaver and Sarachik (1990a) used to determine the salt flux boundary condition (Fig. 2). The symmetric boundary condition at the equator was removed and this steady state was then reflected across the equator and used as an initial condition. All boundary conditions were also reflected about the equator. Experiment 3 was integrated forward for 7204 surface years with one tracer timestep corresponding to 4 days at the surface (12 days at the bottom of the ocean) for the first 60 surface years and to 2 days at the surface (6 days at the bottom) for all subsequent time.

Figure 6 shows the kinetic energy density throughout the long term integration and once more indicates significant variability at the near-decadal period (regions with rapid variation in the curve). The violent overturning flushes, as described by Weaver and Sarachik (1990b) are also clearly evident. In this two-hemisphere run the oscillations occur in each hemisphere, independent of the other hemisphere. For this reason the kinetic energy density does not appear as regular as in Figs. 3, 4a and 5. For example, in times when both hemispheres are in the deep water formation stage of the oscillation, the kinetic energy density appears larger than when one hemisphere is in the deep water formation stage and one hemisphere is in the “reverse-cell” stage (lowest kinetic energy density state of the oscillation). The kinetic energy density of this latter state in turn is larger than in a state when both hemispheres are in the “reverse-cell” stage.

3.4 Experiment 4

Up to this point we have been using the acceleration techniques of Bryan (1984), in which the timestep for integration of the barotropic vorticity and baroclinic velocity equations, differed from the timestep used in the integration of the tracer equations for salinity and temperature. Similarly, longer timesteps were also used at deeper levels in the integration of the tracer equations. One must therefore be careful when talking about timescales associated with asynchronous integrations. In order to see if the decadal oscillation timescale was robust we took the 33 level single hemisphere model of Section

3.2 at year 6188 (in the midst of a period of oscillations — Fig. 5) and changed the timestepping procedure by setting the timestep to 18000 seconds for all variables at all depths (synchronous integration). Figure 7a shows the kinetic energy density throughout the 137 years of integration. The system underwent 16 complete oscillations during this integration giving a period of 8.6 years. In the next section we look at the three dimensional aspects through the particular oscillation of this integration shown in Fig. 7b.

4. The Advective Mechanism for the Decadal Oscillation: **A Three-Dimensional Perspective**

In this section we focus our attention on an 11.41 year portion of the synchronous integration run (Experiment 4). The particular period of interest begins at year 6233.17 (Fig. 7) and represents an *average* oscillation (i.e., not the most or least energetic). Figure 8 illustrates the overturning streamfunction at 1.14 year intervals throughout the single oscillation portrayed in Fig. 7b. In the lowest kinetic energy state of the oscillation the meridional overturning circulation consists of five main features (Fig. 8a):

- 1) A surface trapped near-equatorial cell that is driven by Ekman divergence away from the equator and Ekman convergence to about 28°S where the zonal wind stress changes sign. This particular cell does not vary much with time (Figs. 8a–j)
- 2) A deeper collapsed thermohaline circulation cell with sinking to about 2000 m.
- 3) A polar reverse cell with rising motion near the polar boundary (70° S) that is connected to another near-surface cell which is driven by Ekman convergence/divergence.
- 4) A deep, weak sluggish unventilated cell which diminishes with time (Figs. 8a–d).
- 5) A weak, local cell at great depth near the equatorial boundary. As discussed by Weaver and Sarachik (1990a,b) this cell is spurious in that it is driven by artificial convection generated by sources and sinks of temperature and salinity that occur when the grid Reynolds and Peclet number numerical stability criteria are violated. Once the cell is present it is difficult to remove since it is self-sustaining i.e., associated with the cell are relatively large vertical velocities which continuously violate the grid Reynolds and Peclet criteria. The time scale for this cell to effect the circulation in the basin is diffusive (Weaver and Sarachik, 1990a,b) i.e., several thousand years. It is also very weak and hence plays no role at all. It is still, however, important to point out the reason for its presence in order to understand our model results fully.

As we progress through the oscillation the reverse cell at the polar boundary intensifies (Fig 8b; increasing kinetic energy — Fig. 7b). At the same time the collapsed thermohaline circulation cell also intensifies. This latter cell continues to increase in strength (Fig. 8c) until the reverse cell is gone (Fig. 8d) and deep water is forming at the southern boundary to

5000 m. The influence of the Ekman cell discussed in 3) above is now seen trapped at the surface (Fig. 8d) while the kinetic energy density of the basin is now a maximum (Fig. 7b). The deep water formation stage of the oscillation is not persistent over long periods. As we shall show below, high latitude freshening shuts off convection and the thermohaline circulation begins to collapse (Figs. 8e–g; decreasing kinetic energy in Fig. 7b) until a reverse cell is once more generated at the polar boundary (Fig. 8h; minimum kinetic energy in Fig. 7b). Figures 8i,j show how the reverse cell again intensifies making the system more energetic (Fig. 7b) and the whole process repeats itself again.

In order understand what is causing this thermohaline circulation to change so drastically on the timescale of about 8.6 years we must look at the circulation from a three-dimensional perspective. Figure 9 shows contours of temperature at the top level of the model ($z = 25$ m) at the same 1.14 year intervals illustrated in Fig. 8. Figures 10, 11 and 12 show salinity contours, vertical velocity contours and horizontal velocity vectors at $z = 25$ m, $z = 50$ m and $z = 25$ m, respectively. Horizontal velocity vectors and salinity contours at the 15th model level ($z = 970$ m) are illustrated in Figs. 13 and 14, respectively. For sake of brevity we have only included a plot in Figs. 10–14 corresponding to every second plot of Figs. 8 and 9.

We start our discussion from the stage of the oscillation when deep water is forming (Fig. 8d) and the system is most energetic (Fig. 7b). Figure 9d shows that when deep water is forming the surface contours of temperature do not differ much from the zonally uniform reference temperatures used in the surface boundary condition (Fig. 1b). Most notable exceptions to this are in the western boundary current where advection is important and in the southeastern corner where there is a remnant of the warm (Fig. 9d), saline (Fig. 10b) waters which have risen from below (see later discussion). This latter patch of warm, saline water is soon cooled and eliminated through convection while at the same time a neutrally buoyant warm, saline anomaly begins to develop around 50°S (Fig. 9e), in the region between the subpolar and subtropical gyres, where the wind stress curl changes sign (Fig. 1a). The nature of the salinity surface boundary condition implies net freshening at high latitudes near the eastern boundary (Fig. 2). This high latitude freshening has the effect of shutting off deep water formation by creating a local pool of relatively fresh water between 31.2 and 31.5 ppt at the eastern boundary of the model domain (Fig. 10c — notice that the local minimum centred at about 65°S , 45°E lies under the local maximum of freshening portrayed in Fig. 2). As a result of this net freshening, the thermohaline circulation slowly collapses (Figs. 8f,g). Meanwhile, the warm, saline anomaly grows with time near 50°S (Figs. 9f,g; Fig. 10c) and is advected eastward (Fig. 12c). The actual anomaly forms in a region where there is a local *evaporation* maximum (Fig. 2). Upon reaching the eastern

boundary the warm, saline pool moves poleward (Figs. 9h, 10d) as it is advected by a developing boundary current (Fig. 12c,d). We have now reached the stage where the reverse cell begins to develop at the polar boundary (Figs. 8a–c, h–j).

When the warm, saline pool of subtropical waters reach the eastern boundary and begins to travel polewards it is cooled to the colder overlying *atmospheric* temperature (Fig. 1b). This induces convective overturning so that the warm, saline waters are mixed rapidly to about 1000 m or so. We readily see these warm, saline waters in contour plots at deeper levels. For example, Fig. 14a, b and e show a local maximum in the temperature at a depth of about 970 m. These waters are then advected to the polar boundary (Fig. 13a, b and e), diffusing as they proceed. Upon reaching the polar boundary they rise as they are warmer than the overlying cool surface waters (Fig. 14e, c.f., Fig. 9j). This rising water can be seen in the vertical velocity contour plots of Figs. 11a,b and e, as upwelling along the southern boundary 10–15° off the eastern boundary. Once these waters reach the surface they travel to the southeastern boundary as another boundary current (Fig. 12a, b and e) whereupon they are rapidly cooled and sink to the deep ocean. The local surface temperature and salinity maxima observed in Figs. 9a–d, h–j and Figs. 10 a,b,d,e, respectively, at the southeastern boundary are a direct result of the upwelling of the warm, saline waters whose origin was in the middle of the basin between the subtropical and subpolar gyres. The reverse cell which was seen in Fig. 8 is therefore due to the sinking of these warm, saline waters near 50°S and their subsequent rising at the southern boundary. Since the upwelling occurs along a broad band at the southern boundary it dominates over the intense downwelling at the southeastern corner (Figs. 11a and e) and so in a zonally integrated sense their appears to be upwelling in the upper 1000 m or so at 70°S (Figs. 8a–c, i,j) — the reverse cell. We now proceed to the next stage of the oscillation.

The reverse cell driven by the sinking of the warm, saline waters along the eastern boundary near 50 °S only lasts as long as the surface anomaly persists there. Figures 9b and 9c together with Figs. 9h–j show how the warm anomaly is slowly cooled and eliminated through convection. A similar elimination of the surface salinity anomaly occurs (Figs. 10a and 10b together with Figs. 10d and 10e). The deep warm, saline maximum (Figs. 14a,b,e) slowly drifts westward from the eastern boundary when convection is stopped (Figs. 14c,d). Once the anomaly has been convected away the upwelling along the polar boundary weakens and eventually ceases (lagged by an advection timescale associated with the passage from a particle from 50°S to the southern boundary — see discussion below). A surface salinity and temperature anomaly is left at the southeastern corner (Fig. 9c, d; Fig. 10b) which is quickly eliminated through surface cooling causing deep water to form. High

5. Sensitivity to Vertical Eddy Viscosity

A natural question which one must address is why has such decadal variability not been observed in previous numerical modelling studies — two main reasons exist. The first reason is that researchers often spin up their models using restoring boundary conditions on salinity as well as temperature and then switch to a flux boundary condition for subsequent, relatively short, time integrations. Under restoring boundary conditions, as we discuss briefly in the next section, none of this variability is observed. Short integrations using flux boundary conditions may also not resolve the timescale associated with the variability.

The second and most important reason lies in the fact that researchers often use high values of the vertical eddy viscosity coefficient. As discussed by Killworth (1989), Cox (1989), and Weaver and Sarachik (1990a), to suppress computational modes in equatorial regions one must either use high vertical resolution or a large vertical eddy viscosity coefficient. Since it is often computationally impractical to spin up global models with high vertical resolution, researchers such as Bryan and Lewis (1979), Manabe and Stouffer (1988), and Manabe *et al.* (1990) have used $A_{MV} = 100 \text{ cm}^2\text{s}^{-1}$, Cox (1989) has used $A_{MV} = 50 \text{ cm}^2\text{s}^{-1}$, and Toggweiler *et al.* (1989a, b) have used $A_{MV} = 20 \text{ cm}^2\text{s}^{-1}$. We illustrate the effects of this increased vertical eddy viscosity coefficient by conducting one final experiment.

Experiment 5 (Table 1) is identical to Experiment 1 with the exception that the vertical eddy viscosity coefficient was increased from $A_{MV} = 1 \text{ cm}^2\text{s}^{-1}$ to $A_{MV} = 20 \text{ cm}^2\text{s}^{-1}$ from the onset. This experiment was integrated for 2519 surface (7556 bottom) years by which time a statistically steady state had been reached. Figure 17 shows the kinetic energy density throughout the integration using the same axis scalings as in Fig. 3. The whole system became significantly less energetic and a steady state was obtained. What is readily evident is that the decadal variability was almost entirely suppressed. The only variability occurred during the first several hundred years when the system underwent only a few weak oscillations.

6. Discussion

In this paper we have presented evidence for the existence of significant internal variability at near decadal period in a fully nonlinear, primitive equation ocean general circulation model. We were able to show that this variability was characterized by oscillations involving the turning on and shutting off of deep water formation which in turn were associated with the propagation of warm, saline anomalies, generated in the mid-ocean between the sub-polar and sub-tropical gyres, to the eastern boundary. The oscillation timescale is set by advection and is given by the length of time it takes a particle to be advected from the the mid-ocean region, between the subpolar and subtropical gyres, to the eastern boundary and then, as subsurface flow, towards the southern wall. In more complicated geometry one would expect this timescale to be slightly longer since the advective path would no longer be in straight lines.

A knowledge of such internal variability is important in the understanding of the observed oceanic variability. In an attempt to explain variability in the ocean it is most common to seek variability in the external forcing variables. For example, one might try and correlate observed sun spot activity with known oceanographic decadal variability in order to explain the existence of such oceanographic variability. This analysis may well yield erroneous, high correlations which are simply due to two independent parameters varying at similar frequencies. Furthermore, care must also be used in interpreting short time series of observed oceanographic parameters which do not well resolve the decadal timescale. Changes which may be found in such time series could be part of an internal, decadal variability within the system and may not necessarily indicate long term trends.

In the context of climate change we showed that during the oscillation, the poleward heat transport associated with the thermohaline circulation changed by as much as a factor of three at certain latitudes. The maximum poleward heat transport occurred in the state of the oscillation when deep water was forming. This state was very similar to the oceanic component of one of the two stable equilibria in the coupled oceanic-atmospheric model of Manabe and Stouffer (1988). Minimum poleward heat transport occurred in the state when the thermohaline circulation was collapsed. Indeed this state was in turn similar to the oceanic component of the other stable equilibria which Manabe and Stouffer (1988) found. The decadal variability herein can therefore be thought of as an oscillation between the two oceanic states calculated by Manabe and Stouffer (1988) with about an 8.6 year period.

None of the results which we have described in this paper are observed in models which use restoring boundary conditions on both salinity and temperature. When such a boundary condition is used on salinity there is a direct feedback between oceanic surface

salinities and the salinity flux into or out of the ocean. This has the effect of forcing the surface salinity to be zonally uniform, similar to that which we obtained for temperature, and hence anomalies do not form. Similarly, the variability is almost entirely suppressed by the use of high vertical eddy viscosity coefficients often required for the satisfaction of numerical stability criteria.

Acknowledgements

The authors are indebted to M. Cox at GFDL, Princeton for providing them with a copy of the GFDL Bryan-Cox OGCM. This research was supported by an NSERC Operating Grant awarded to AJW, by cooperative agreement number NA85ABH000031 of the Joint Institute for the Study of the Atmosphere and Ocean (University of Washington) and by a grant from the NOAA Office of Climate and Atmospheric Research to the University of Washington Experimental Climate Forecast Center. The interesting discussions that AJW had with Drs. F. Bretherton, G. Mertz, L. Mysak, S. Power, T. Stocker and D. Wright are gratefully acknowledged. The calculations were done on the University of Washington's IBM3090-300.

References

- Bryan, F., 1987: Parameter sensitivity of primitive equation ocean general circulation models. *Journal of Physical Oceanography*, **17**, 970–985.
- Bryan, K., 1969: A numerical method for the study of the circulation of the world ocean. *Journal of Computational Physics*, **4**, 347–376.
- Bryan, K., 1979: Models of the world ocean. *Dynamics of Atmospheres and Oceans*, **3**, 327–338.
- Bryan, K., 1984: Accelerating the convergence to equilibrium of ocean-climate models. *Journal of Physical Oceanography*, **14**, 666–673.
- Bryan, K., and M.D. Cox, 1972: An approximate equation of state for numerical models of ocean circulation. *Journal of Physical Oceanography*, **2**, 510–514.
- Bryan, K., L.J. Lewis, 1979: A water mass model of the world ocean. *Journal of Geophysical Research*, **84**, 2503–2517.
- Cox, M.D., 1984: A primitive equation, three-dimensional model of the ocean. GFDL Ocean Group Technical Report No. 1.
- Cox, M.D., 1987: Isopycnal diffusion in a z-coordinate ocean model. *Ocean Modelling*, **74**, 1–5.
- Cox, M.D., 1989: An idealized model of the world ocean. Part I: The global-scale water masses. *Journal of Physical Oceanography*, **19**, 1730–1752.
- Dickson, R.R., J. Meincke, S-A Malmberg and A.J. Lee, 1988: The “Great Salinity Anomaly” in the northern North Atlantic 1968–1982. *Progress in Oceanography*, **20**, 103–151.
- Gill, A.E., 1982: *Atmosphere-Ocean Dynamics*. Academic Press, 662 pp.
- Haney, R.L. 1971: Surface thermal boundary condition for ocean circulation models. *Journal of Physical Oceanography*, **1**, 241–248.
- Ikeda, M., 1990: Decadal oscillations of the air-ice-ocean system in the northern hemisphere. *Atmosphere-Ocean*, **28**, 106–139.
- James, I.N., and P.M. James, 1989: Ultra-low-frequency variability in a simple atmospheric circulation model. *Nature*, **342**, 53–55.
- Killworth, P.D., 1989: On the parameterisation of deep convection in ocean models. In: *“Aha Huliko a” : Parameterization of small scale processes*, P. Müller, ed., Hawaii Institute of Geophysics.
- Lazier, J.R.N., 1980: Oceanographic conditions at Ocean Weather Ship BRAVO, 1944–1974. *Atmosphere-Ocean*, **18**, 227–238.

- Levitus, S., 1982: Climatological Atlas of the World Ocean. *NOAA Professional Paper* 13. US Department of Commerce: National Oceanic and Atmospheric Administration.
- Manabe, S., and R.J. Stouffer, 1988: Two stable equilibria of a coupled ocean-atmosphere model. *Journal of Climate*, **1**, 841–866.
- Manabe, S., K. Bryan and M.J. Spelman, 1990: Transient response of a global ocean-atmosphere model to a doubling of atmospheric carbon dioxide *Journal of Physical Oceanography*, **20**, 722–749.
- Mysak, L.A., and D.K. Manak 1989: Arctic sea-ice extent and anomalies, 1953–1984. *Atmosphere-Ocean*, **27**, 376–405.
- Mysak, L.A., D.K. Manak and R.F. Marsden, 1990: Sea-ice anomalies in the Greenland and Labrador Seas during 1901–1984 and their relation to an interdecadal Arctic climate cycle. *Climate Dynamics*, submitted.
- Stouffer, R.J., S. Manabe and K. Bryan, 1989: Interhemispheric asymmetry in climate response to a gradual increase of atmospheric CO₂. *Science*, **342**, 660–662.
- Toggweiler, J.R., K. Dixon and K. Bryan, 1989a: Simulations of radiocarbon in a coarse-resolution world ocean model 1. Steady state prebomb distributions. *Journal of Geophysical Research*, **94**, 8217–8242.
- Toggweiler, J.R., K. Dixon and K. Bryan, 1989b: Simulations of radiocarbon in a coarse-resolution world ocean model 2. Distributions of bomb-produced Carbon 14. *Journal of Geophysical Research*, **94**, 8243–8264.
- Washington, W.M. and G.A. Meehl, 1989: Climate sensitivity due to increased CO₂: Experiments with a coupled atmosphere and ocean general circulation model. *Climate Dynamics*, **4**, 1–38.
- Weaver, A.J., and E.S. Sarachik, 1990a: On the importance of vertical resolution in certain ocean general circulation models. *Journal of Physical Oceanography*, **20**, 600–609.
- Weaver, A.J., and E.S. Sarachik, 1990b: The role of mixed boundary conditions in numerical models of the ocean's climate. *Journal of Physical Oceanography*, Modelling of the General Circulation of the Ocean Special Edition, submitted.
- Welander, P., 1986: Thermohaline effects in the ocean circulation and related simple models. In: *Large-Scale Transport Processes in Oceans and Atmosphere*, D.L.T. Anderson and J. Willebrand, eds., NATO ASI series, Reidel.

Table 1 Characteristics of the four experiments conducted under mixed boundary conditions.

Experiment Number	Number of Vertical Levels	Number of Hemispheres	Synchronous (S) or Asynchronous (A) integration	Vertical Eddy Viscosity A_{MV} (cm^2s^{-1})	Length of Integration in Surface Years	Length of Integration in Bottom Years
1	12	1	A	1	10760	32279
2	33	1	A	1	3888	11664
3	33	2	A	1	7204	21613
4	33	1	S	1	137	137
5	12	1	A	20	2519	7556

Table 2 Vertical spacing used in the 12 and 33 level model experiments. All depths are in meters.

Model Layer	Depth of Middle	Depth of Bottom	Δz	Depth of Middle	Depth of Bottom	Δz
1	25	51	51	25	50	50
2	85	119	68	75	100	50
3	170	220	100	125	150	50
4	295	371	151	175	200	50
5	483	595	224	225	250	50
6	755	915	320	275	300	50
7	1131	1347	433	325	350	50
8	1623	1898	551	375	400	50
9	2229	2559	661	430	460	60
10	2935	3311	752	495	530	70
11	3721	4131	820	570	610	80
12	4566	5000	869	655	700	90
13				750	800	100
14				855	910	110
15				970	1030	120
16				1095	1160	130
17				1230	1300	140
18				1375	1450	150
19				1535	1620	170
20				1715	1810	190
21				1915	2020	210
22				2135	2250	230
23				2375	2500	250
24				2625	2750	250
25				2875	3000	250
26				3125	3250	250
27				3375	3500	250
28				3625	3750	250
29				3875	4000	250
30				4125	4250	250
31				4375	4500	250
32				4625	4750	250
33				4875	5000	250

Figure Captions

Figure 1. a)— Surface zonal wind stress (dynes/cm²) used to force the model. The meridional wind stress was everywhere zero. b)— Zonal mean restoring temperature (°C) used in the linear damping condition at the surface. c)— Zonal mean restoring salinity (ppt) used in the linear damping condition at the surface in the model of Weaver and Sarachik (1990a).

Figure 2. Salinity flux in mg m⁻²s⁻¹ used as a surface boundary condition. This flux was diagnosed from 52 years of further integration of the steady state of Weaver and Sarachik (1990a).

Figure 3. Kinetic energy density in 10⁻¹ kg m⁻¹s⁻² for the long term 12 level integration (Experiment 1) under mixed boundary conditions.

Figure 4. a)— Blow up of Fig. 3 between 1500 (4500) and 2000 (6000) surface (bottom) years of integration illustrating the near decadal oscillation. b)— The stage in the oscillation when a reverse cell emanates from the southern boundary at 1684 surface (5051 bottom) years. c)— the collapsed state of the oscillation at 1697 surface (5092 bottom) years; d)— the deep water formation state of the oscillation at 1711 surface (5133 bottom) years. The plots in b), c) and d) are taken over several different oscillations.

Figure 5. Kinetic energy density in 10⁻¹ kg m⁻¹s⁻² for the long term 33 level integration (Experiment 2) under mixed boundary conditions

Figure 6. Kinetic energy density in 10⁻¹ kg m⁻¹s⁻² for the long term two hemisphere 33 level integration (Experiment 3) under mixed boundary conditions.

Figure 7. a)— Kinetic energy density in 10⁻¹ kg m⁻¹s⁻² for the 33 level synchronous integration run showing the 8.6 year period oscillation; b)— Kinetic energy density of the single oscillation studied closely in Section 4.

Figure 8. Meridional overturning streamfunction through the decadal oscillation discussed in Section 4 a) 46.77 years; b) 47.91 years; c) 49.05 years; d) 50.19 years; e) 51.33 years; f) 52.47 years; g) 53.62 years; h) 54.76 years; i) 55.90 years; j) 57.04 years after the switch to synchronous integration. The corresponding kinetic energy density is illustrated in Fig. 7b. Positive contours imply clockwise transport.

Figure 9. Contours of temperature in °C at a depth of 25 m a) 46.77 years; b) 47.91 years; c) 49.05 years; d) 50.19 years; e) 51.33 years; f) 52.47 years; g) 53.62 years; h) 54.76 years; i) 55.90 years; j) 57.04 years after the switch to synchronous integration.

Figure 10. Contours of salinity in ppt at a depth of 25 m a) 47.91 years; b) 50.19 years; c) 52.47 years; d) 54.76 years; e) 57.04 years after the switch to synchronous integration.

Figure 11. Contours of vertical velocity in $10^{-3} \text{ cm s}^{-1}$ at a depth of 50 m a) 47.91 years; b) 50.19 years; c) 52.47 years; d) 54.76 years; e) 57.04 years after the switch to synchronous integration. The contour interval is $1 \times 10^4 \text{ cm/s}$.

Figure 12. Velocity vectors at a depth of 25 m a) 47.91 years; b) 50.19 years; c) 52.47 years; d) 54.76 years; e) 57.04 years after the switch to synchronous integration.

Figure 13. Velocity vectors at a depth of 970 m a) 47.91 years; b) 50.19 years; c) 52.47 years; d) 54.76 years; e) 57.04 years after the switch to synchronous integration.

Figure 14. Contours of temperature in $^{\circ}\text{C}$ at a depth of 970 m a) 47.91 years; b) 50.19 years; c) 52.47 years; d) 54.76 years; e) 57.04 years after the switch to synchronous integration.

Figure 15. Poleward heat transport in petawatts (10^{15} Watts) through the single oscillation of Fig. 7b. Refer to Fig. 8 for the corresponding meridional mass transport streamfunction.

Figure 16. Schematic diagram of the advective path that a particle takes from the region between the subpolar and subtropical gyres where the initial anomaly is formed to the place of deep water formation. The broken line indicates a subsurface advective path. Typical advection velocities and associated piecewise advection timescales are also given.

Figure 17. Kinetic energy density in $10^{-1} \text{ kg m}^{-1} \text{ s}^{-2}$ for the 12 level integration using increased vertical viscosity ($A_{MV} = 20 \text{ cm}^2 \text{ s}^{-1}$) under mixed boundary conditions. This experiment is otherwise identical to Experiment 1 discussed in Section 3.1. The axes on the diagram are drawn so as to be the same scale as in Fig. 3.

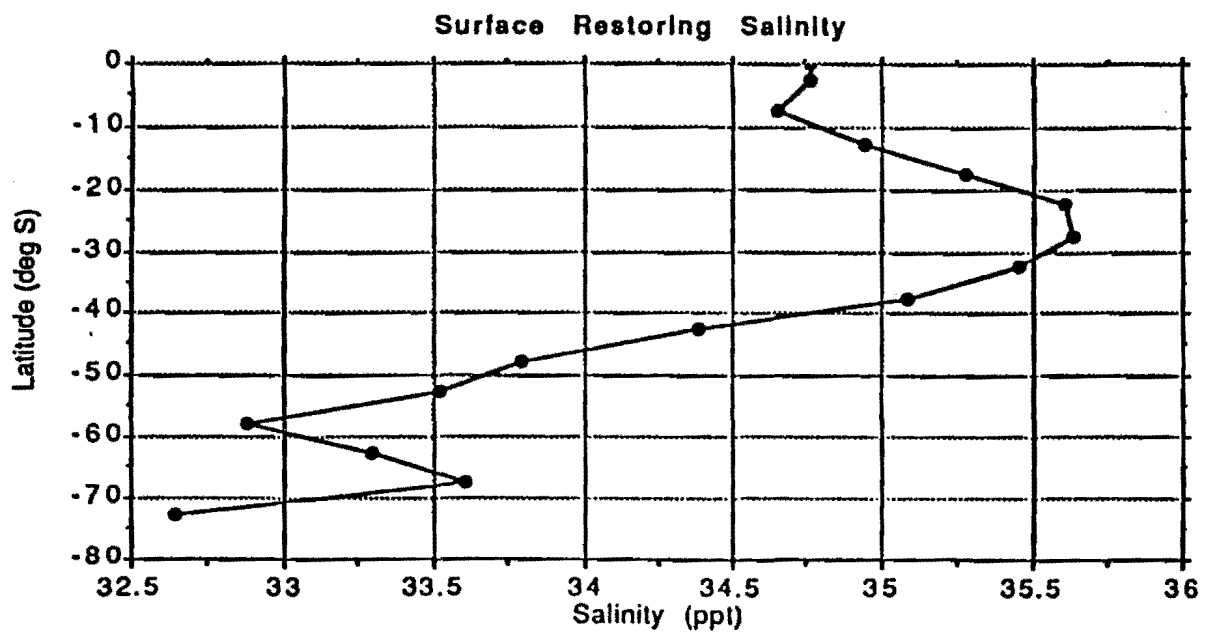
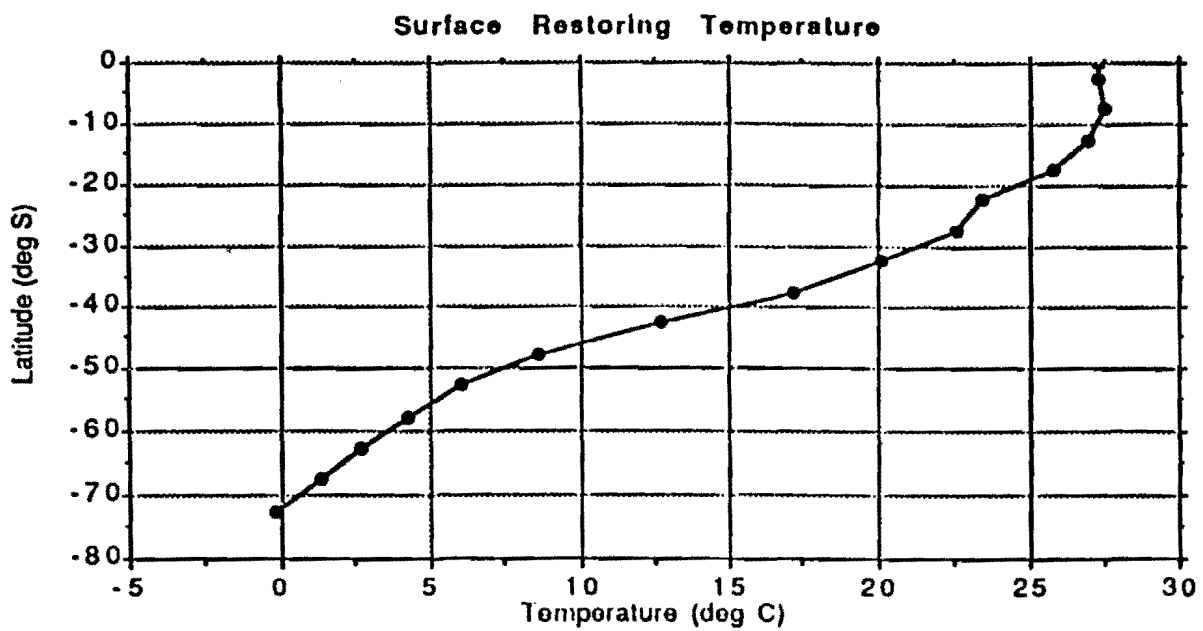
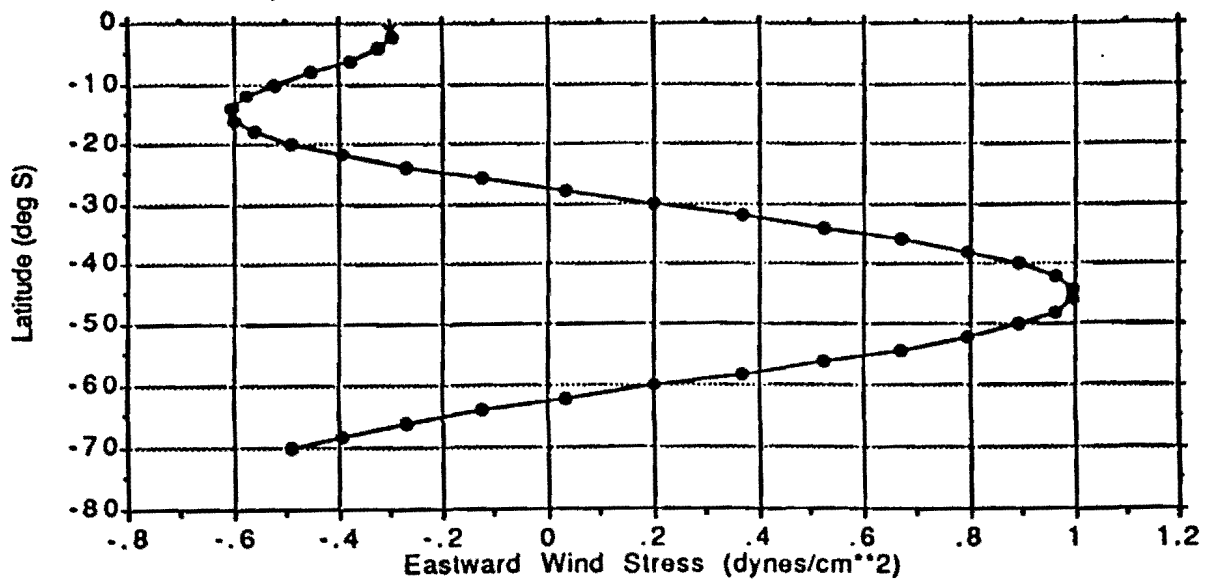


Fig. 1.

Salinity Flux Averaged Over 52 Years

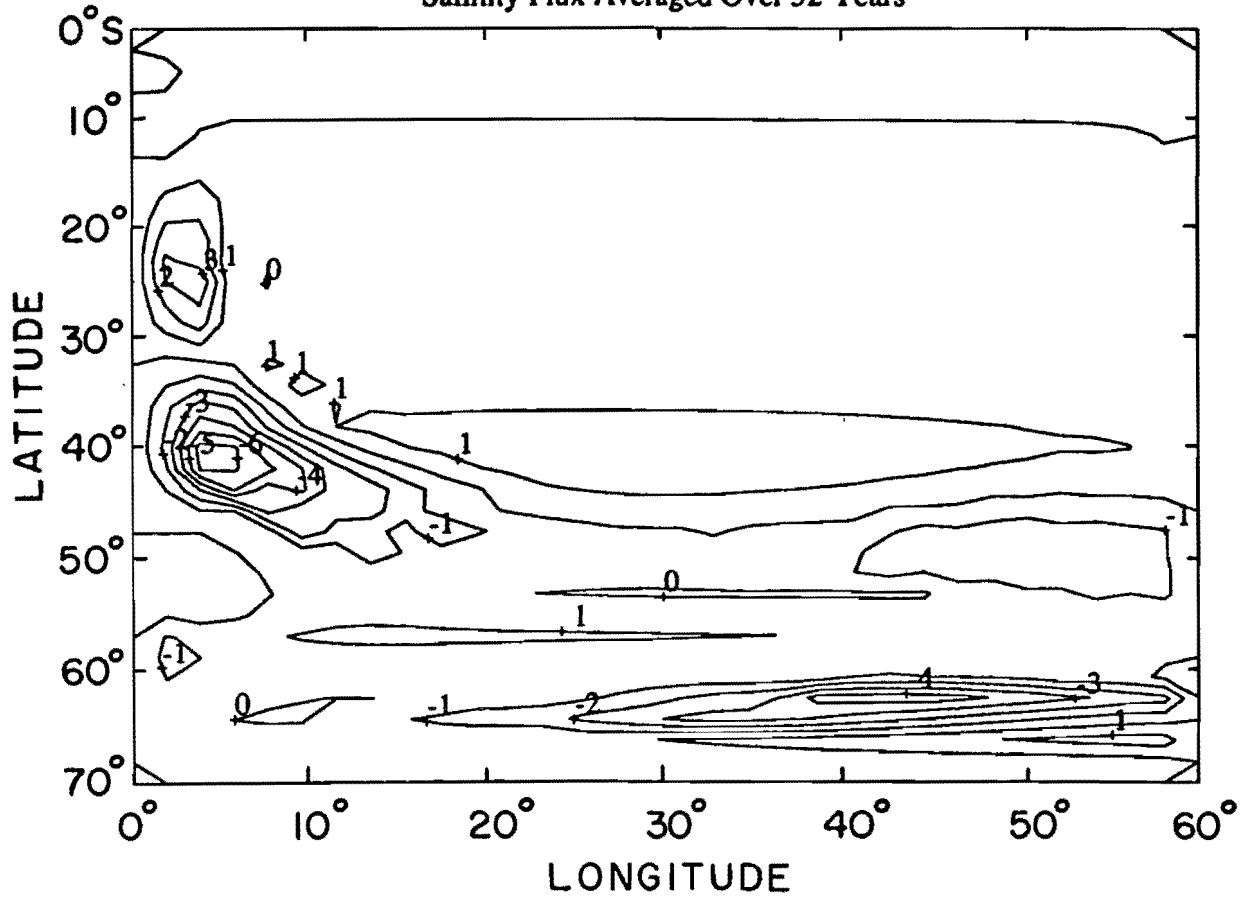


Fig. 2.

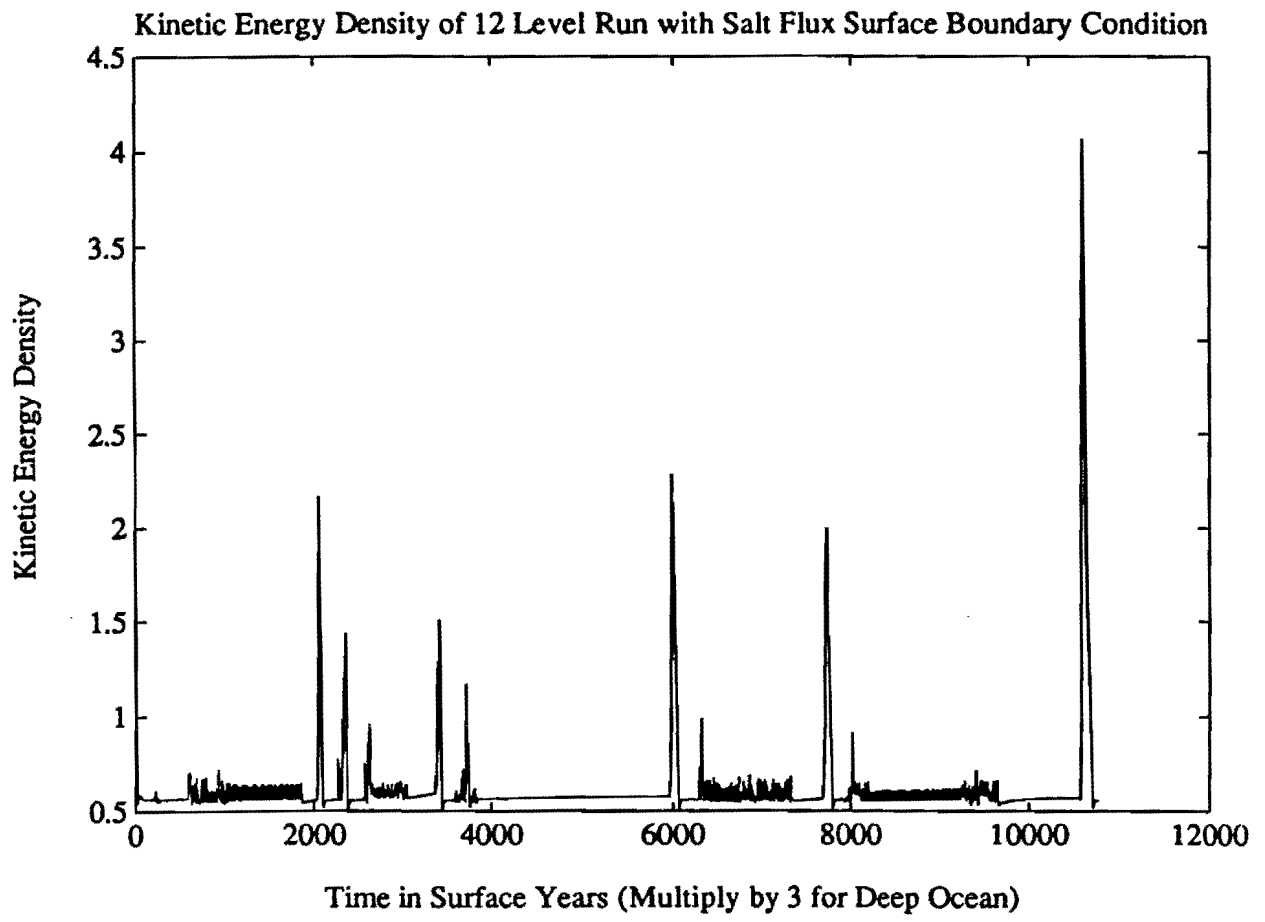
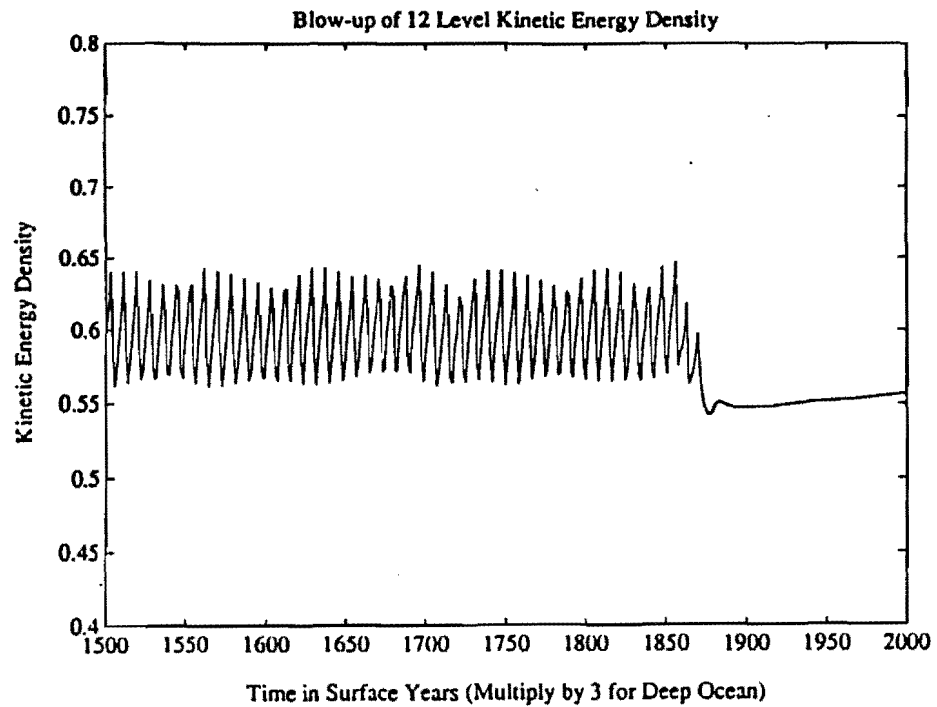
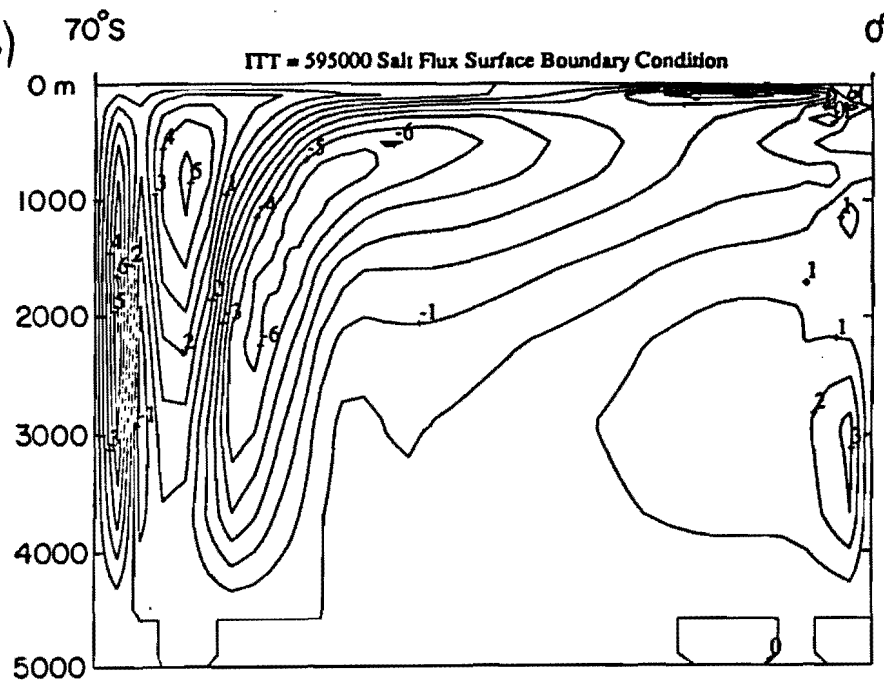


Fig.3.

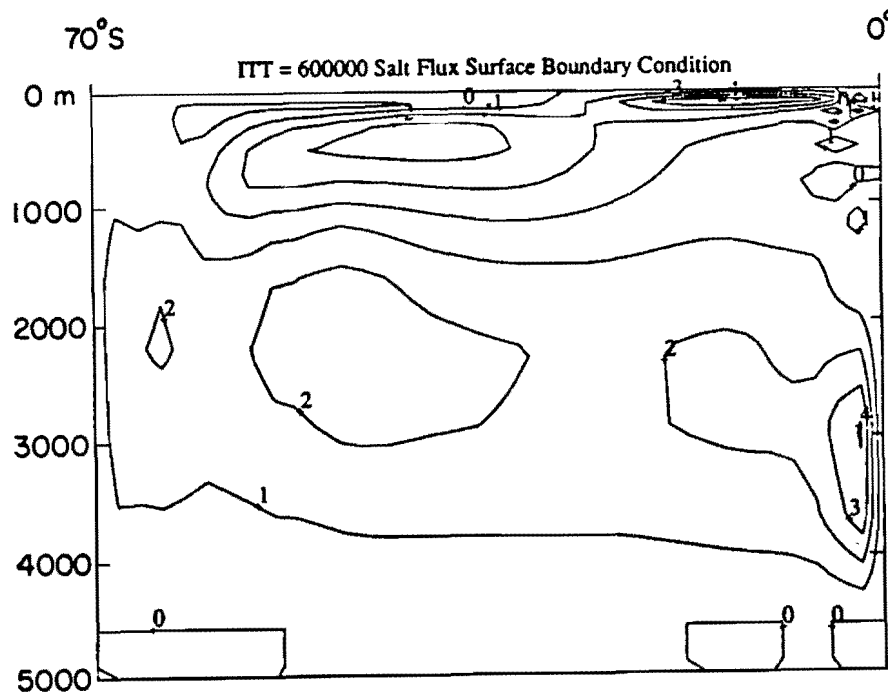
a)



b)



c)



d)

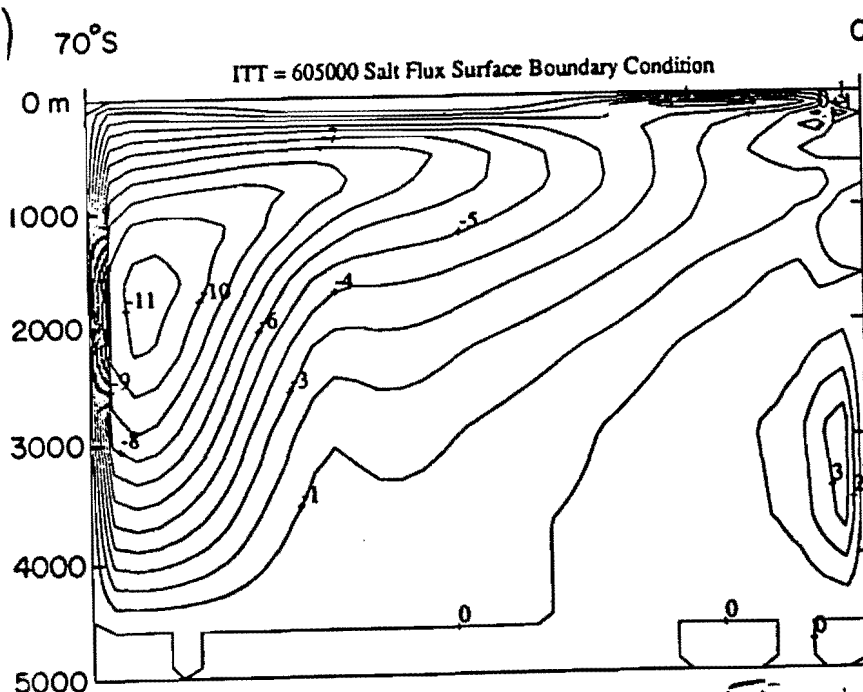
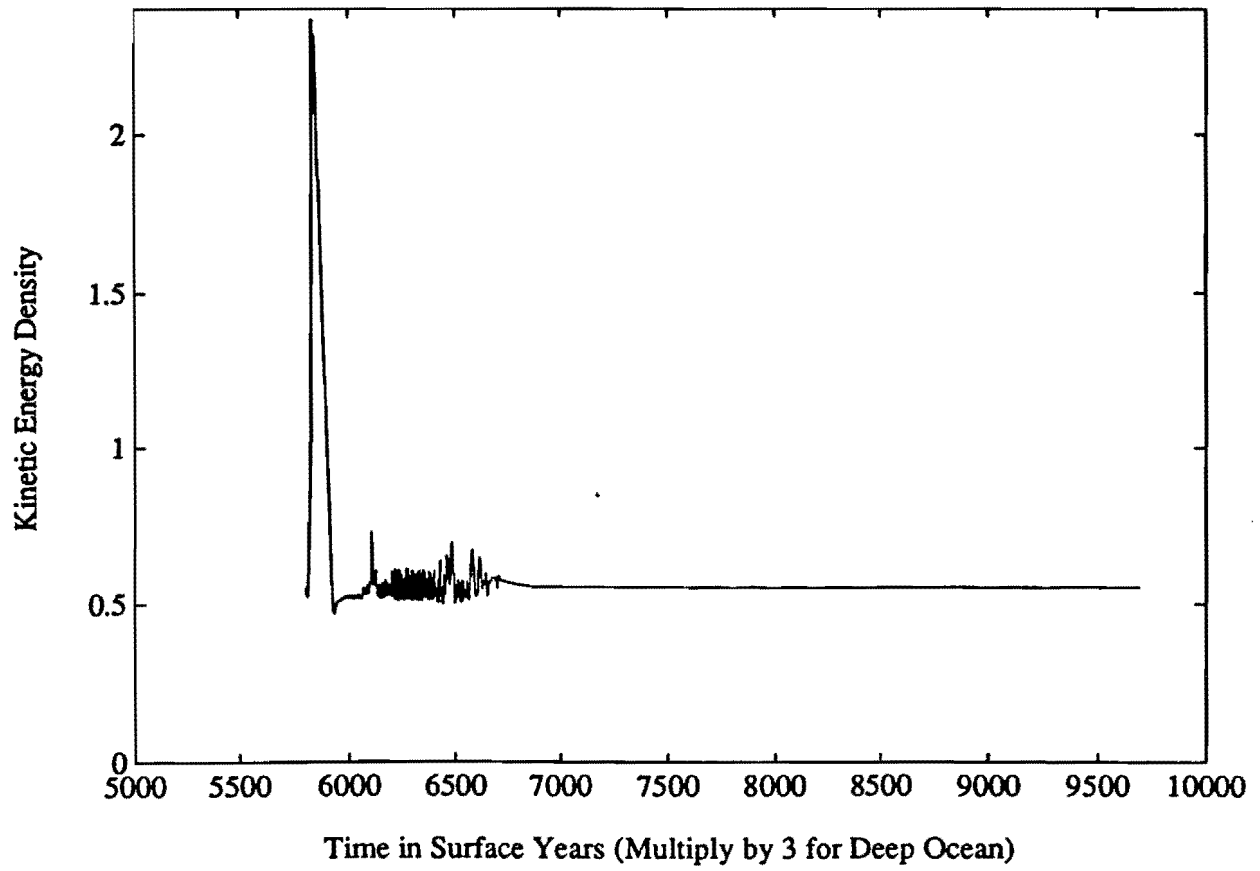


Fig 4.

Kinetic Energy Density of 33 Level Run with Salt Flux Boundary Conditions



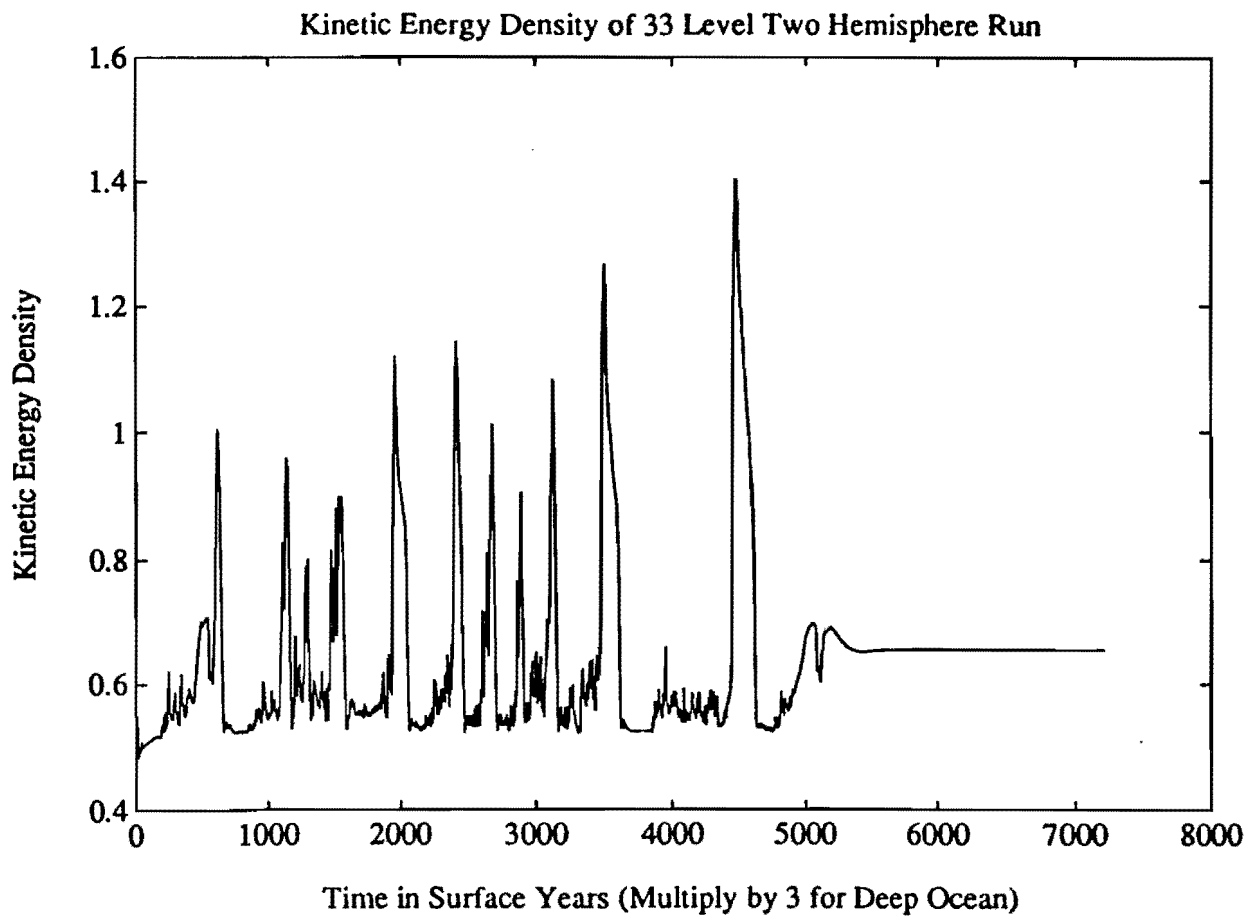
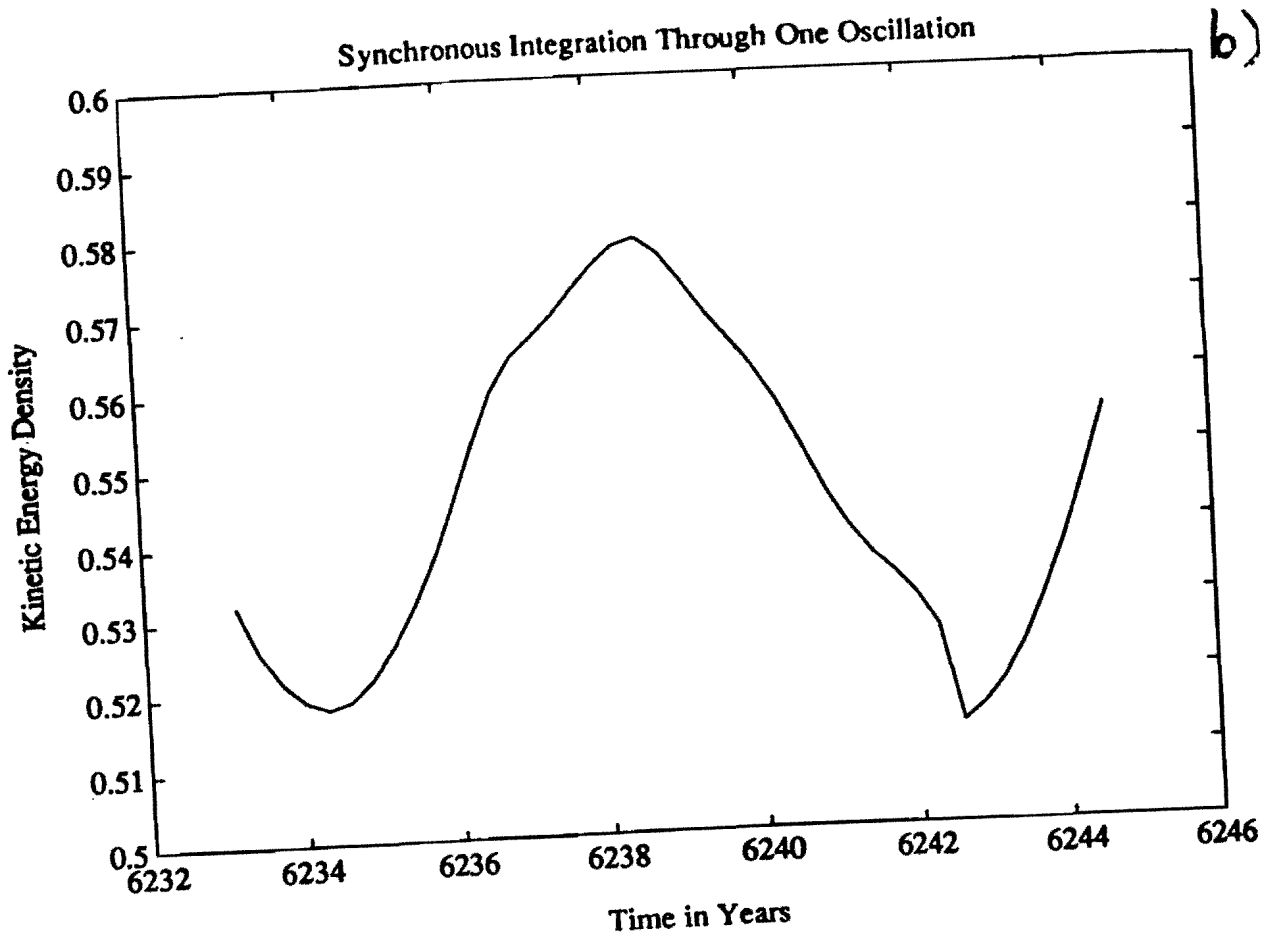
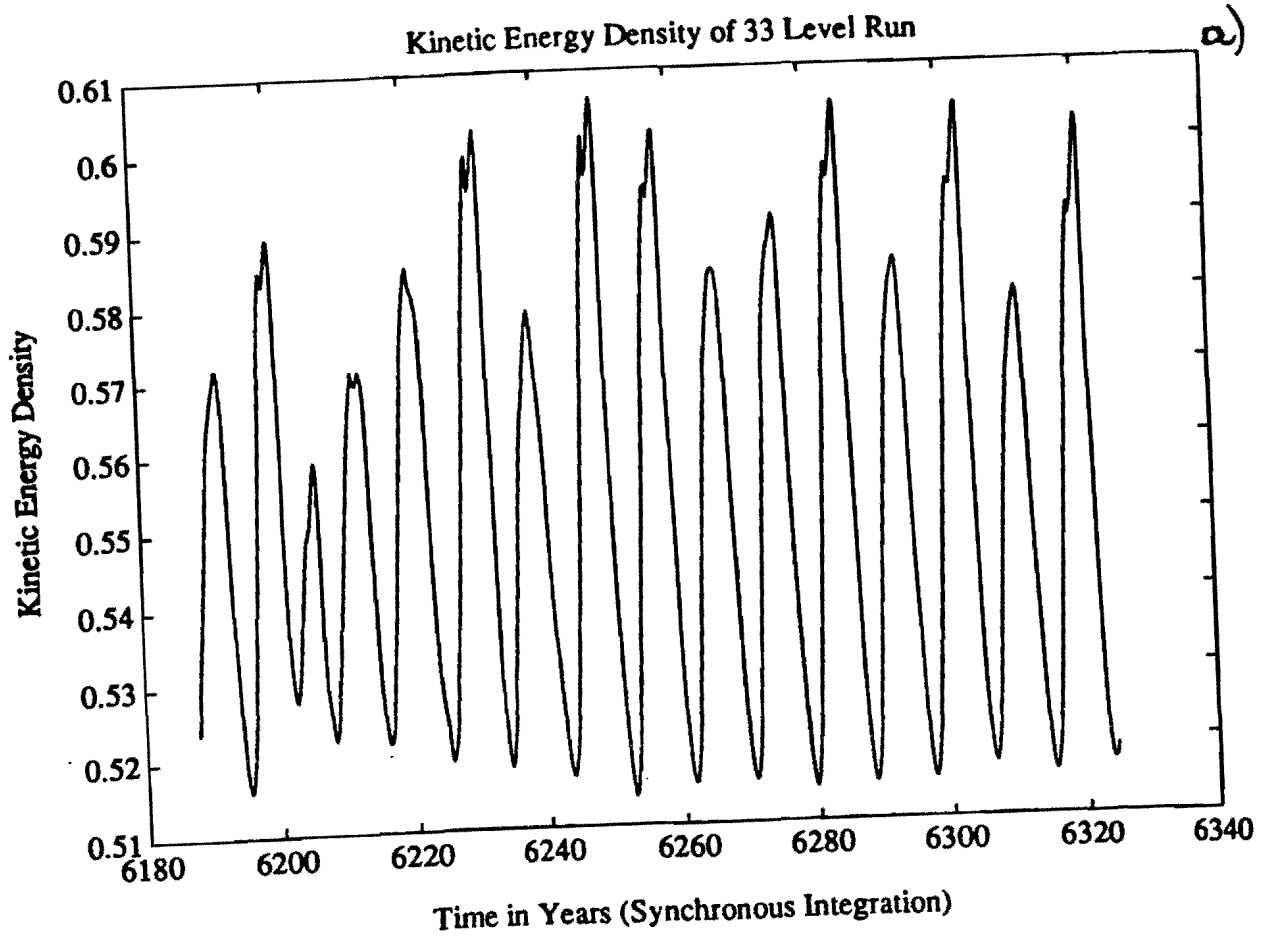


Fig. 6



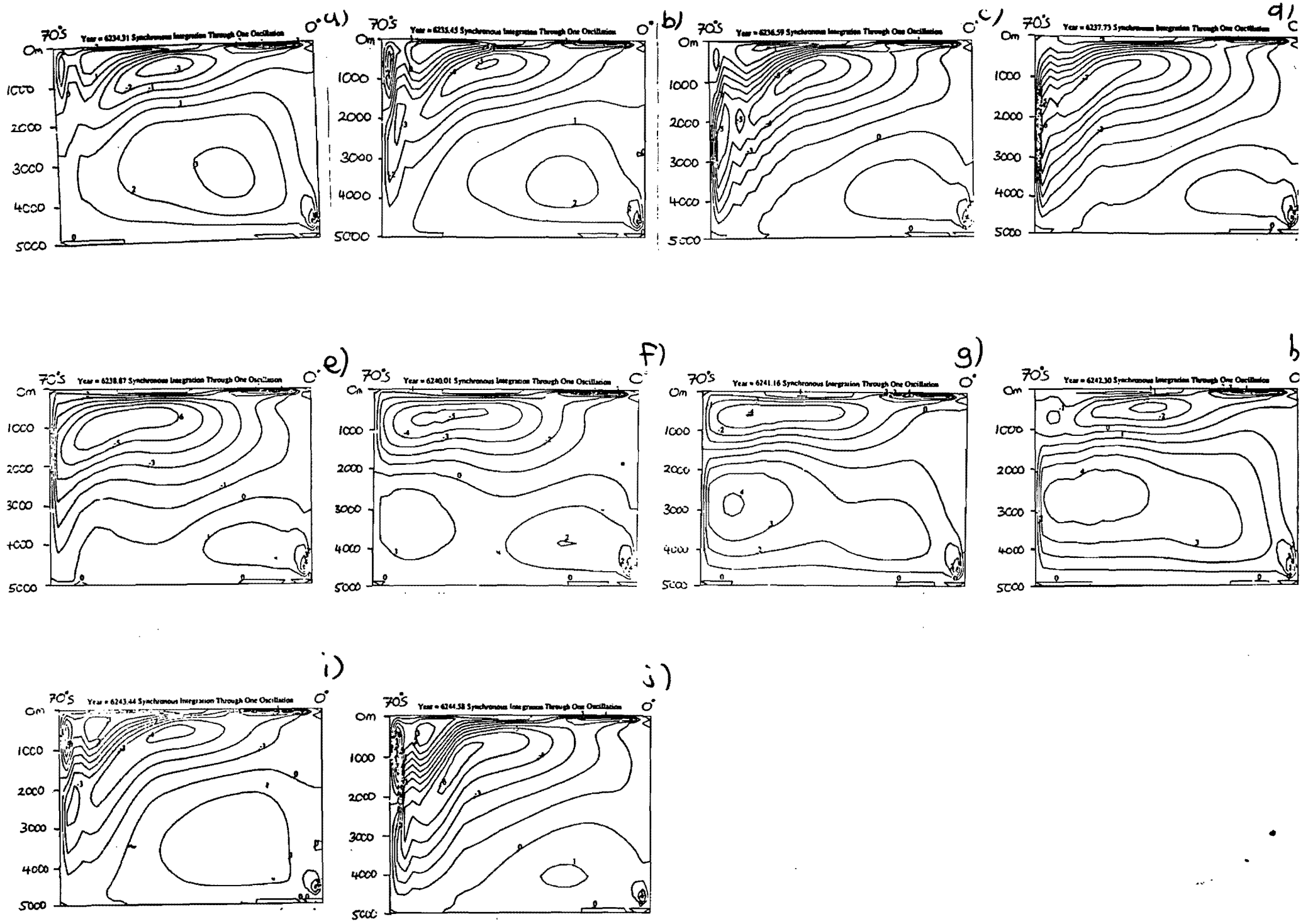


Fig. 8.

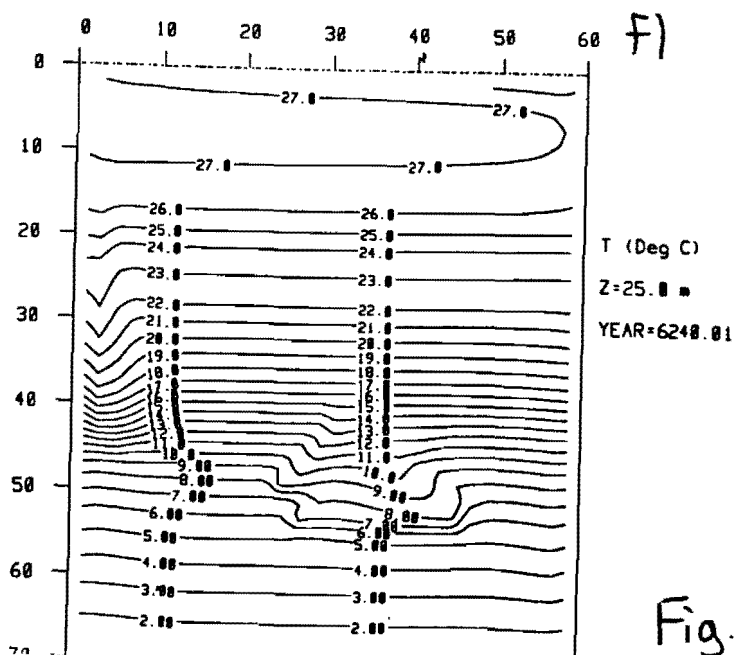
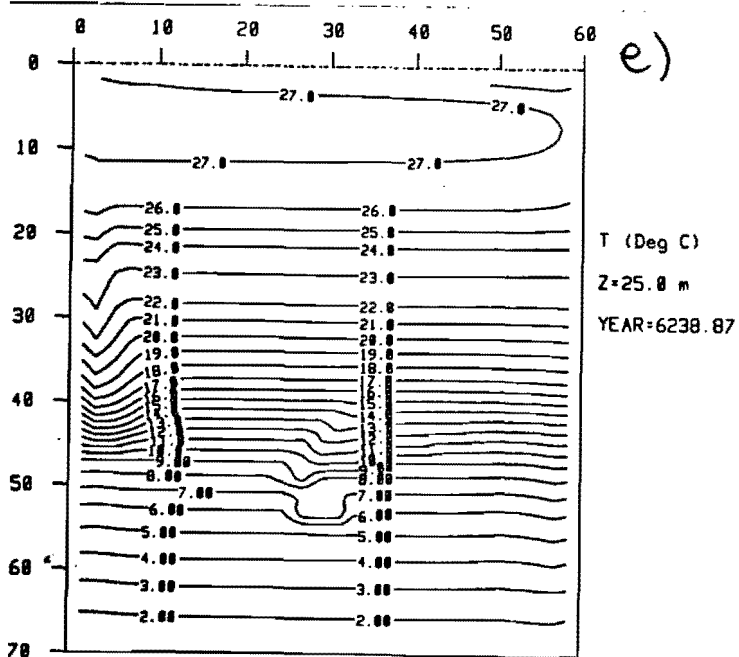
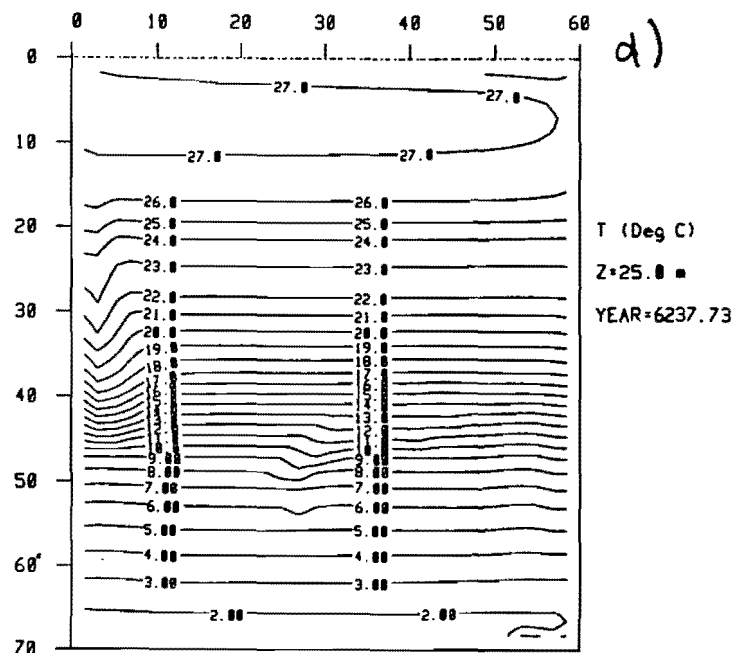
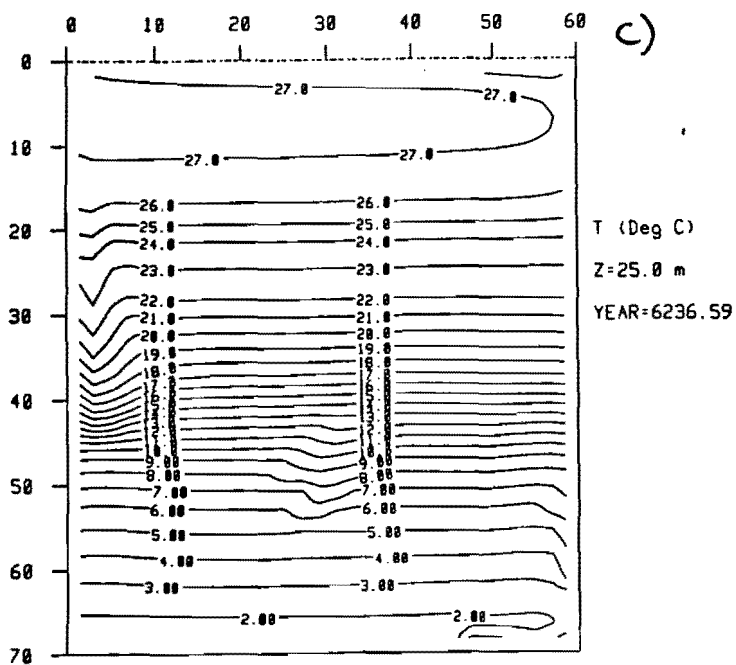
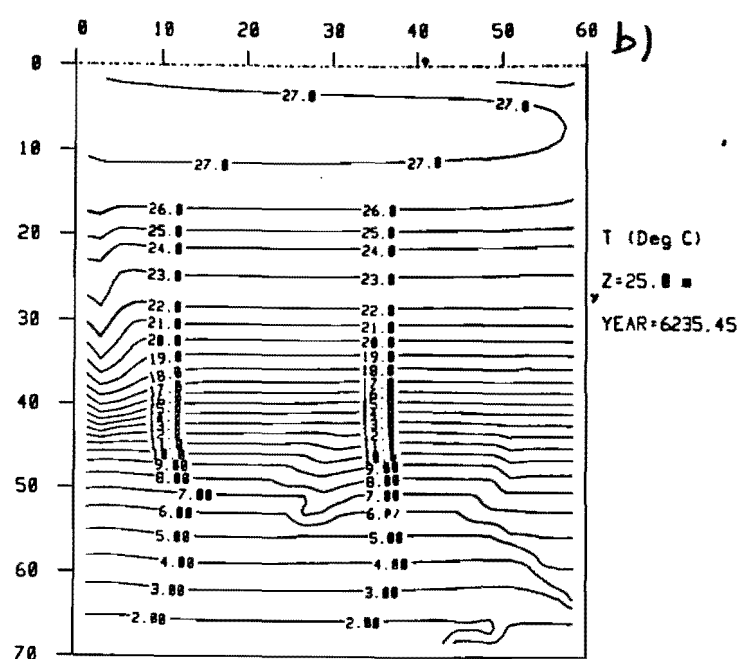
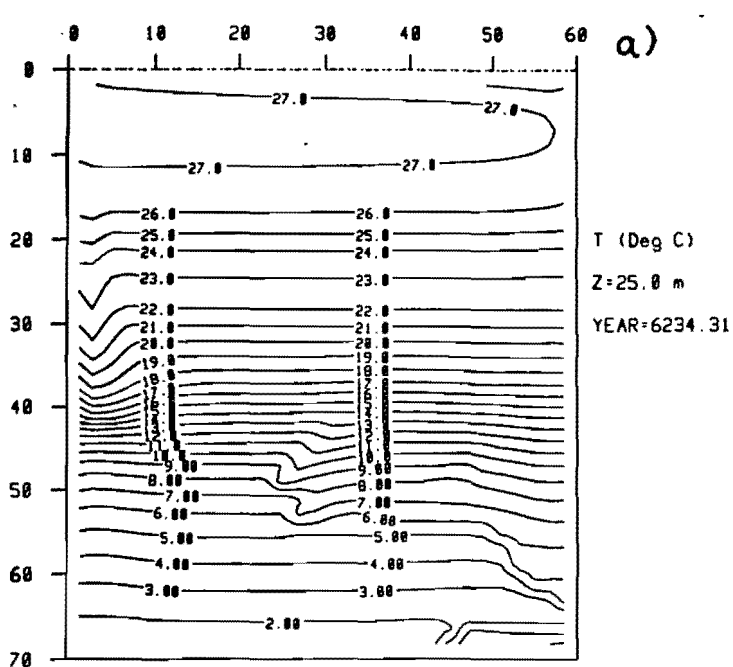
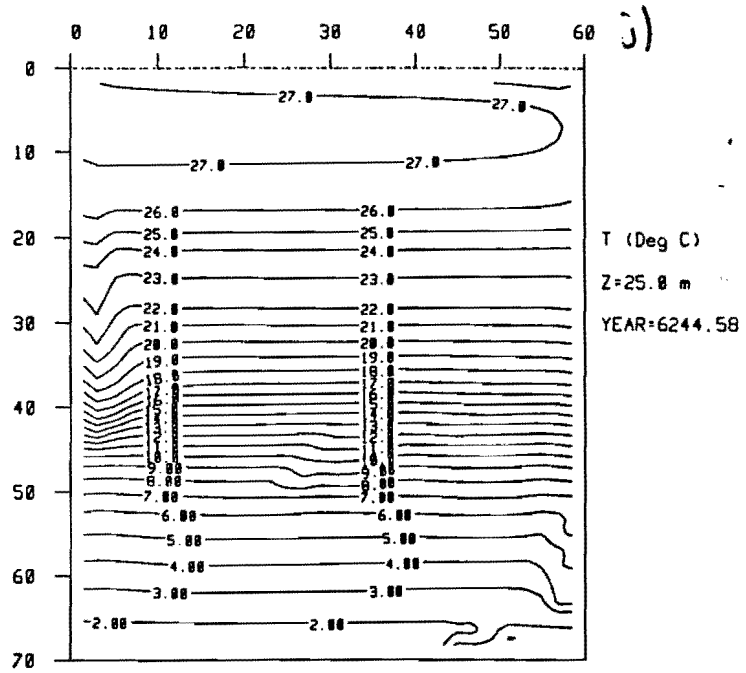
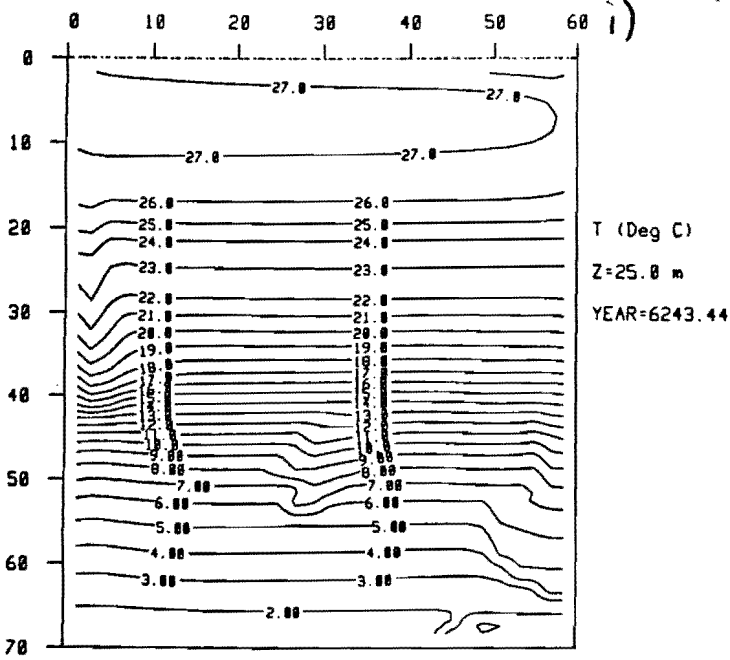
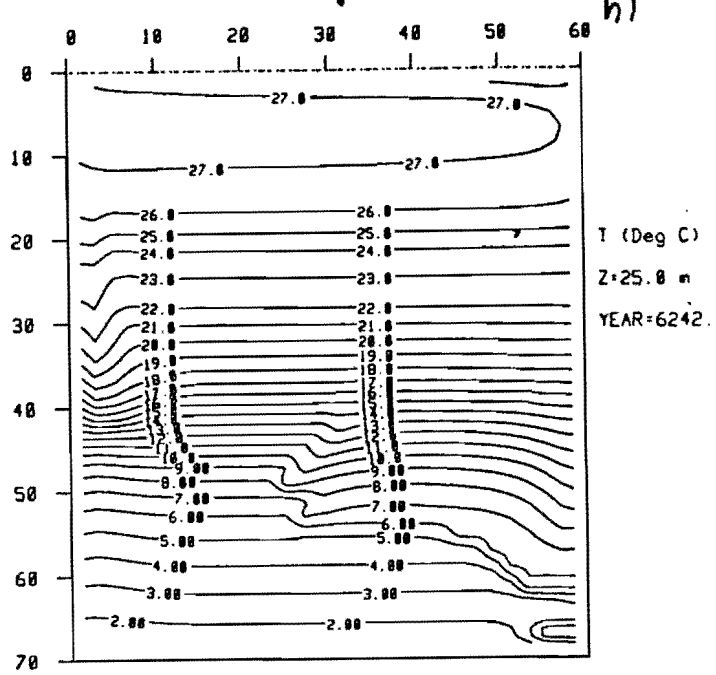
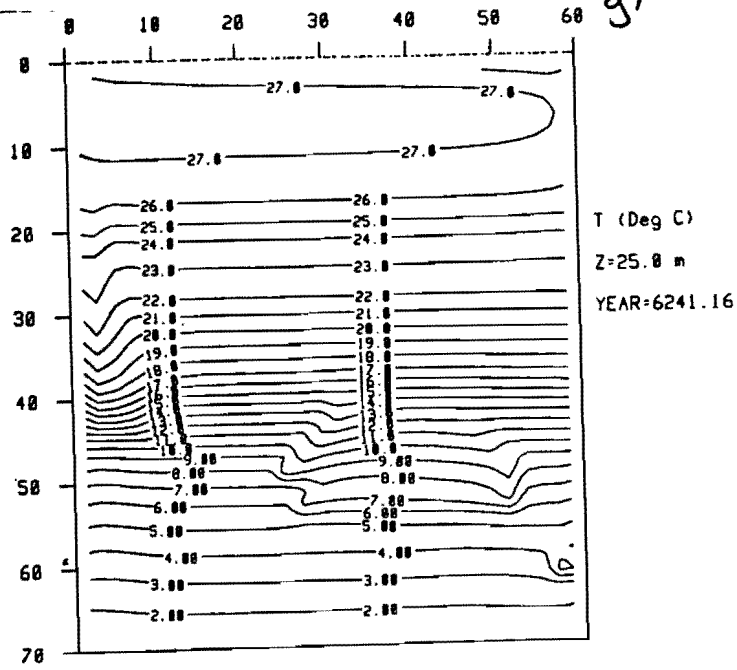


Fig. 9.



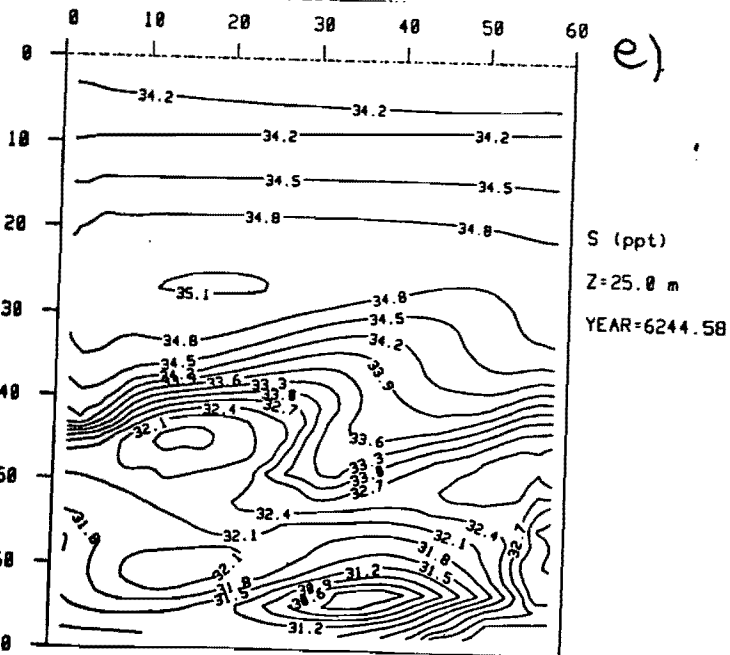
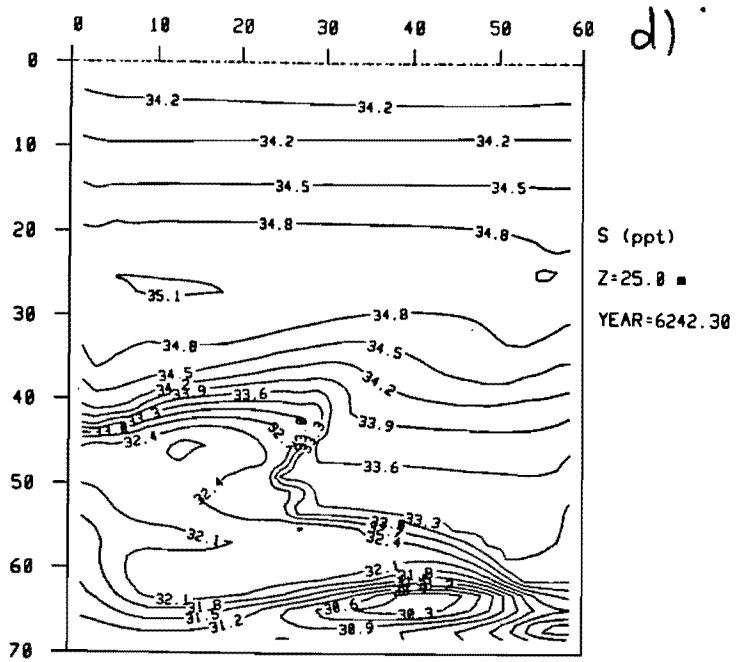
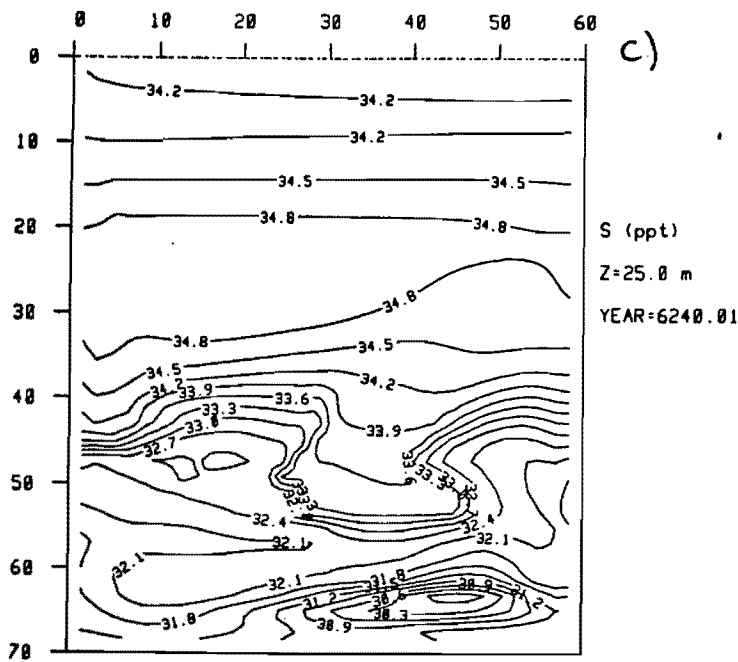
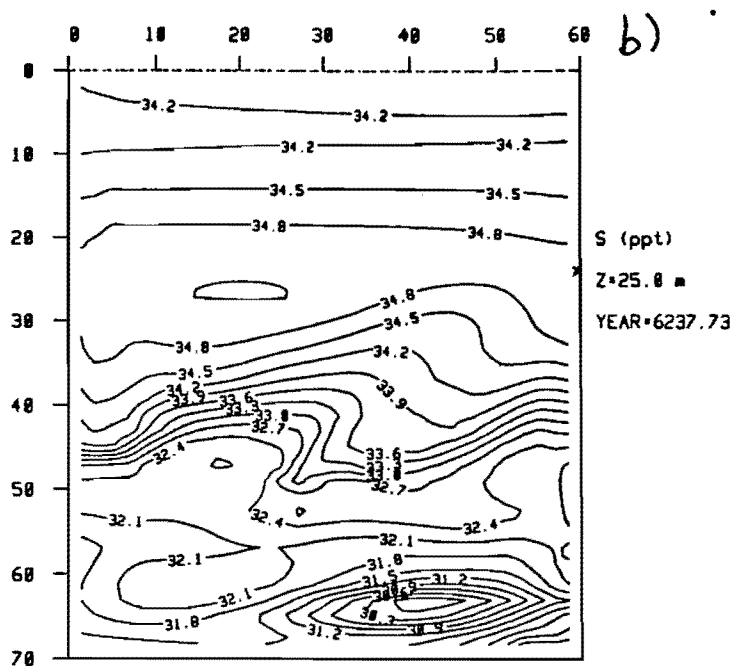
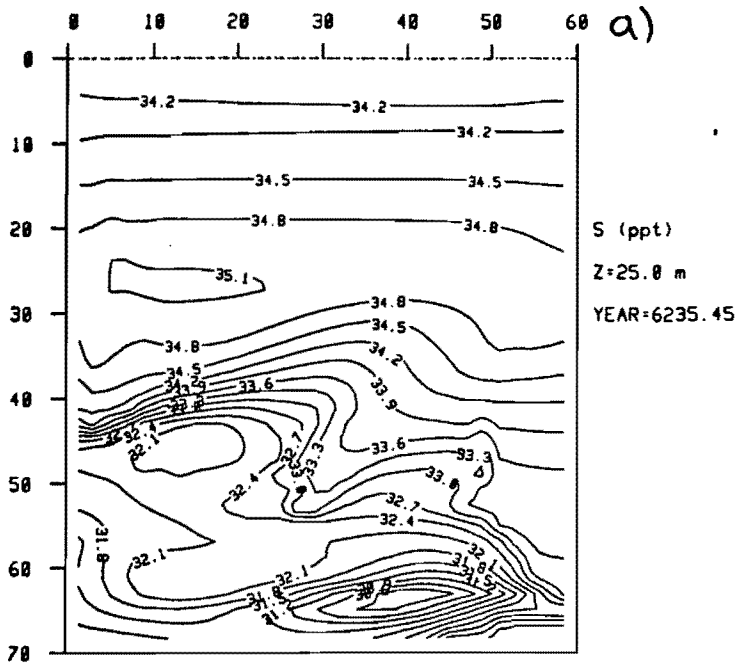
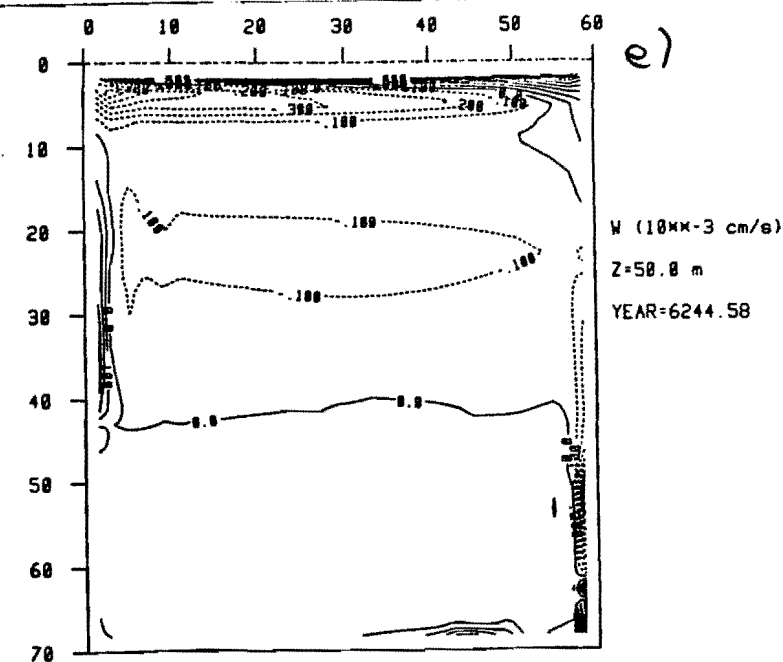
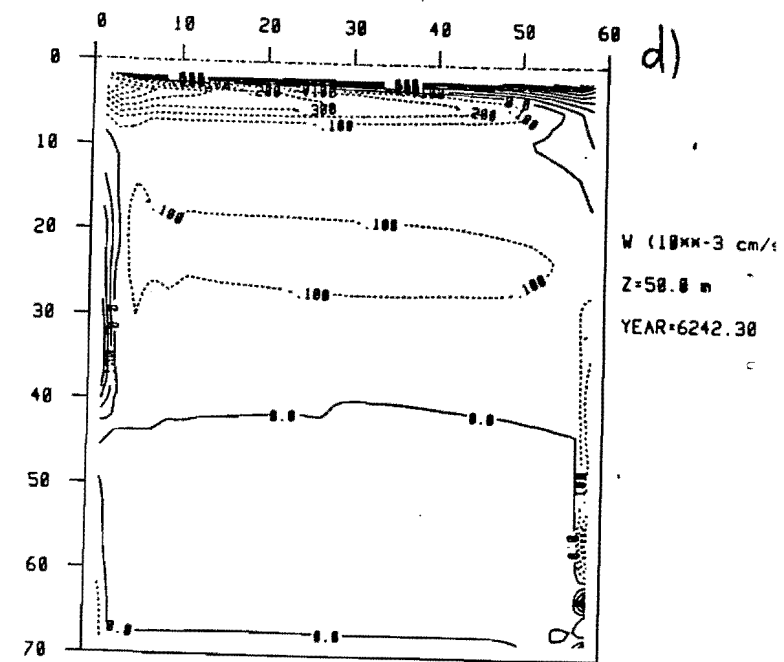
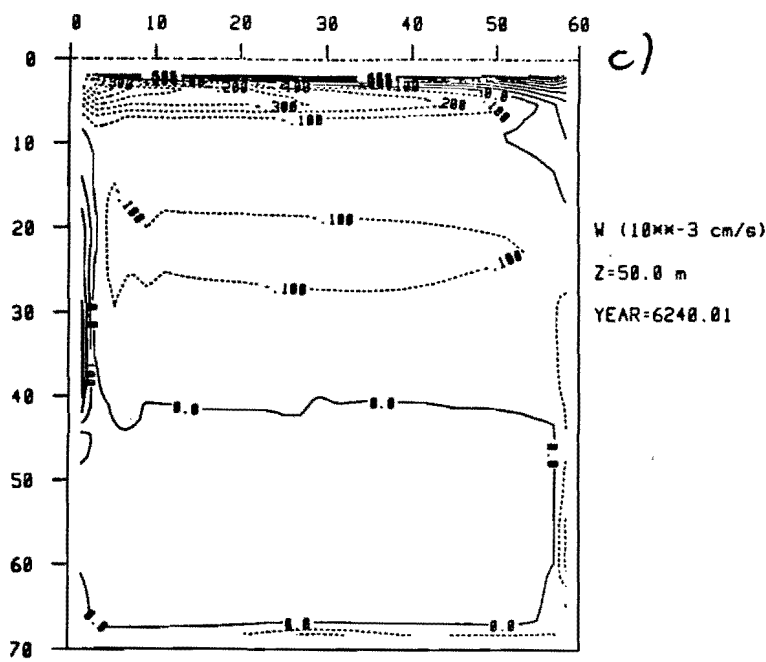
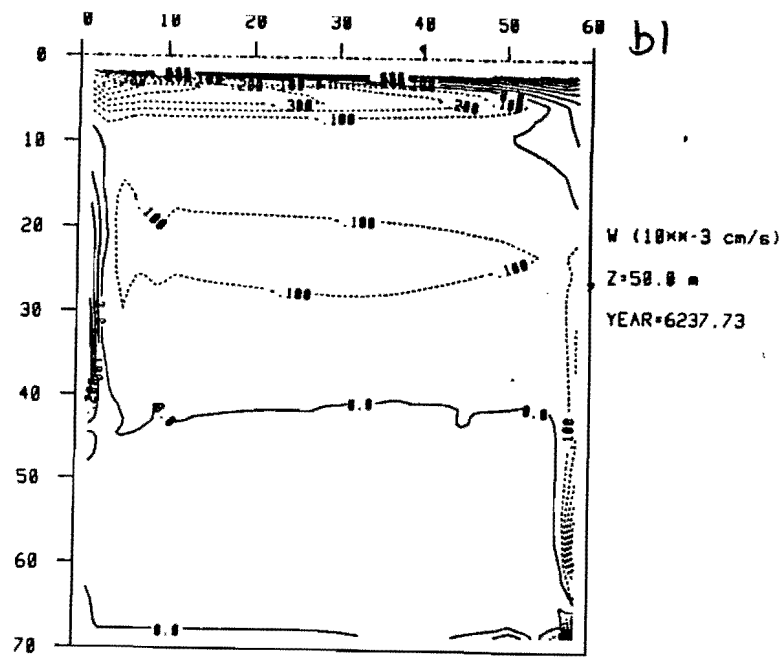
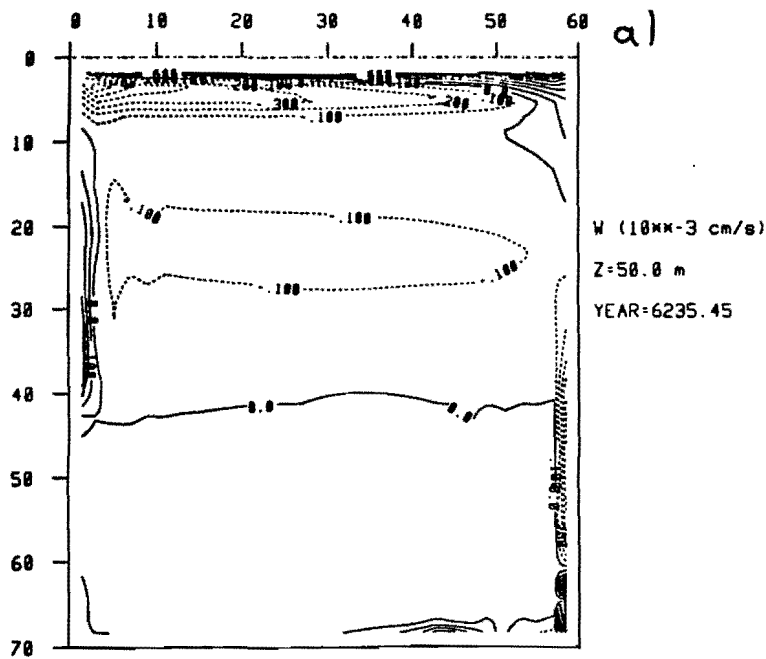


Fig.10.



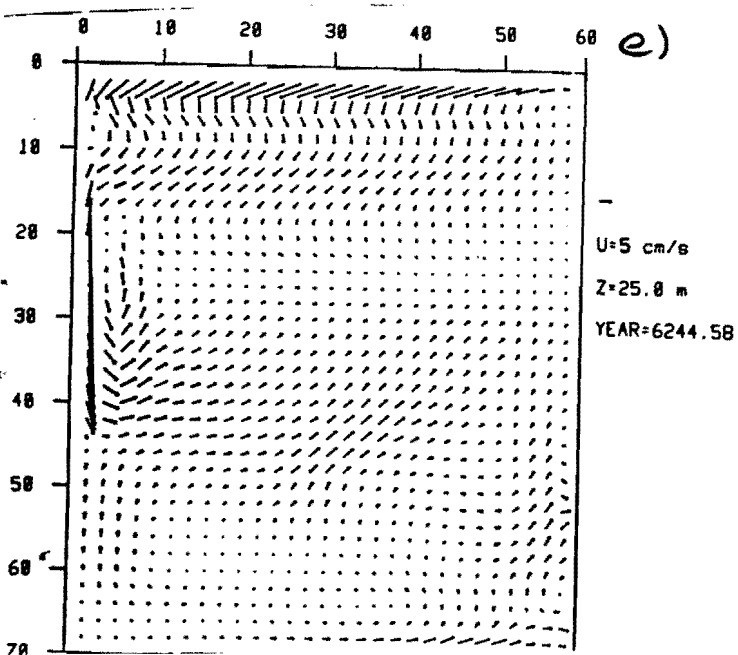
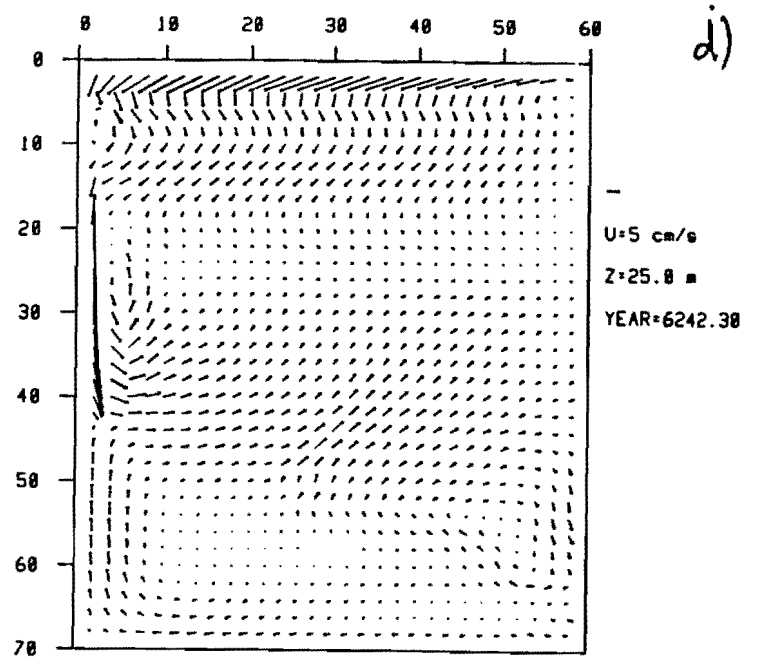
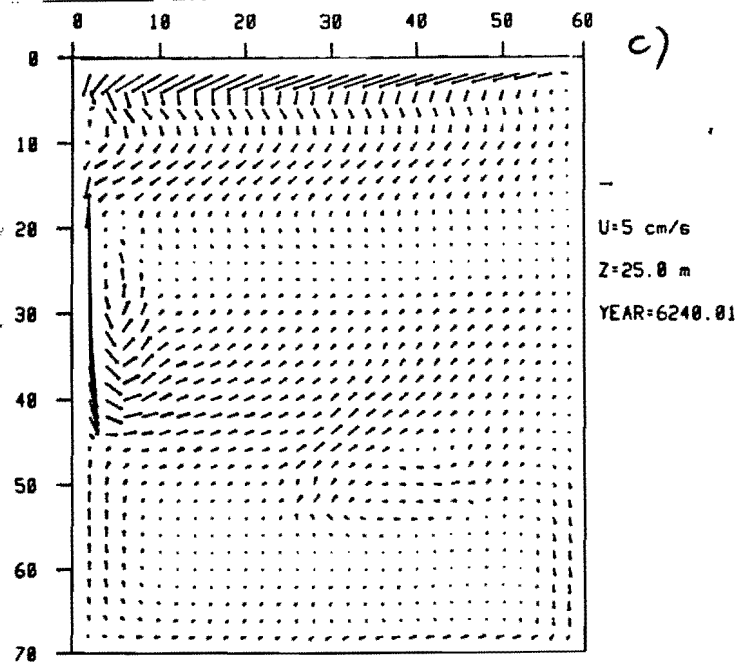
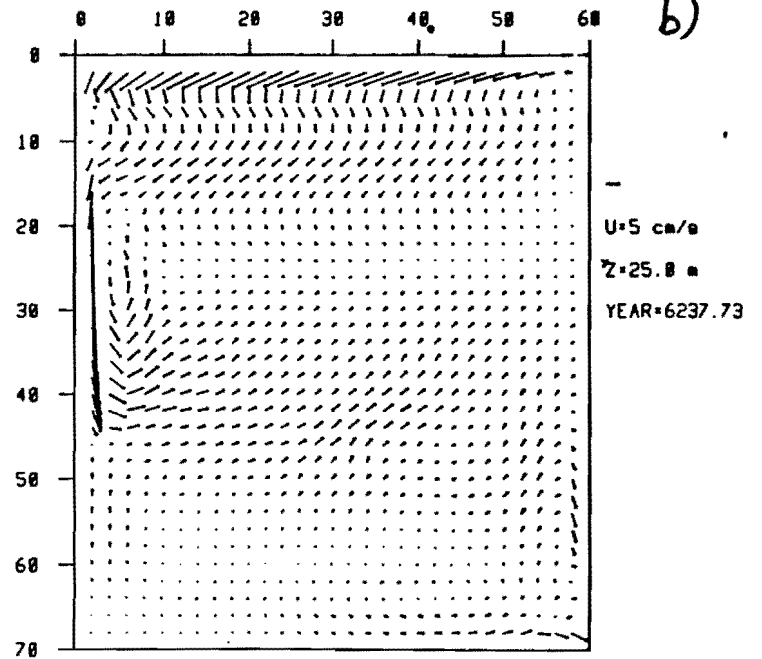
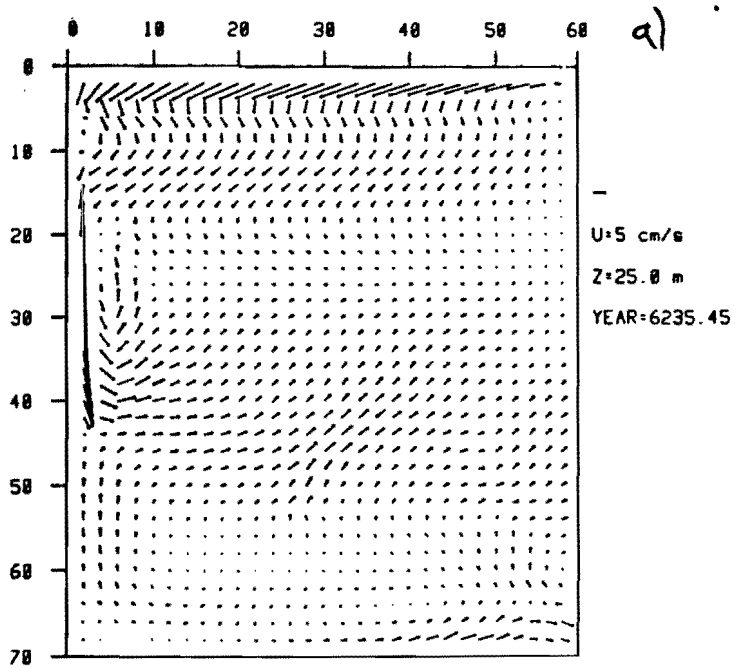


Fig. 12

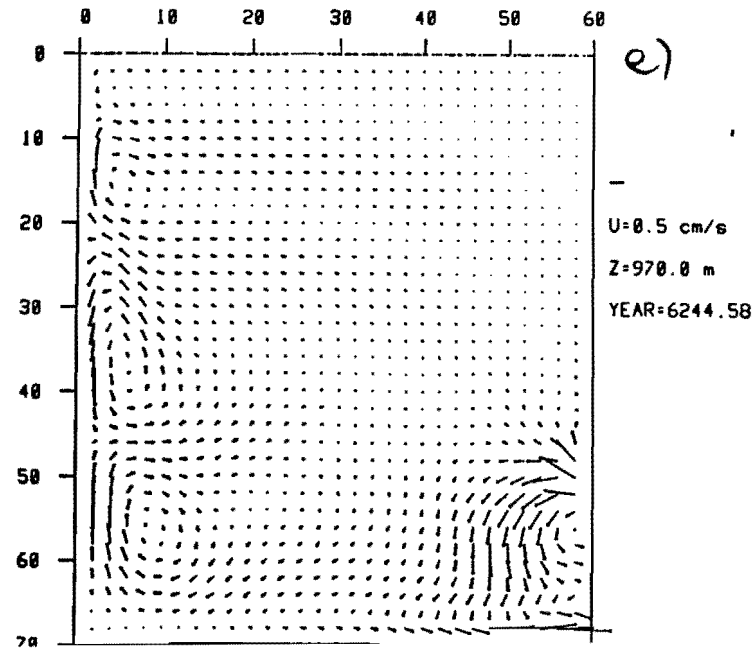
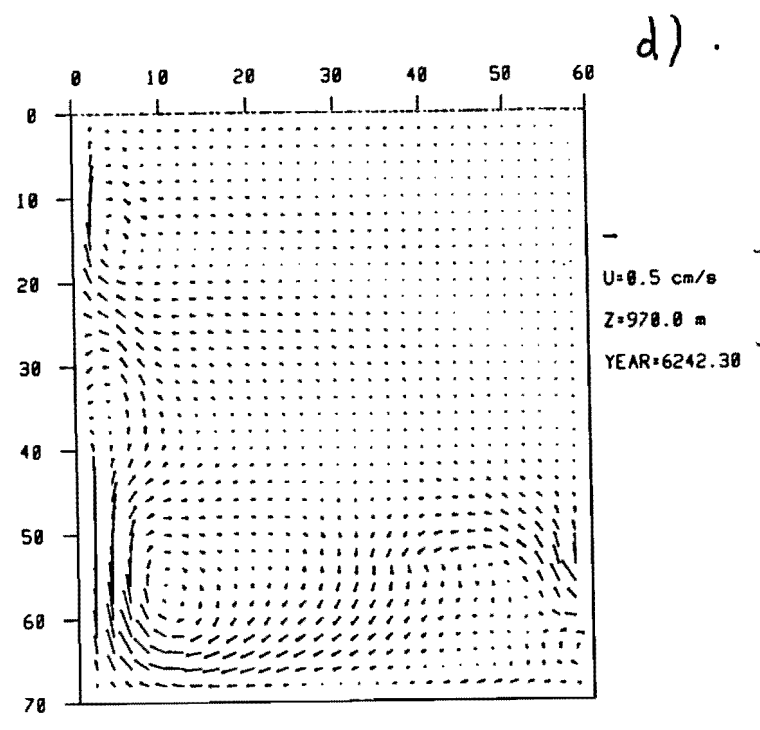
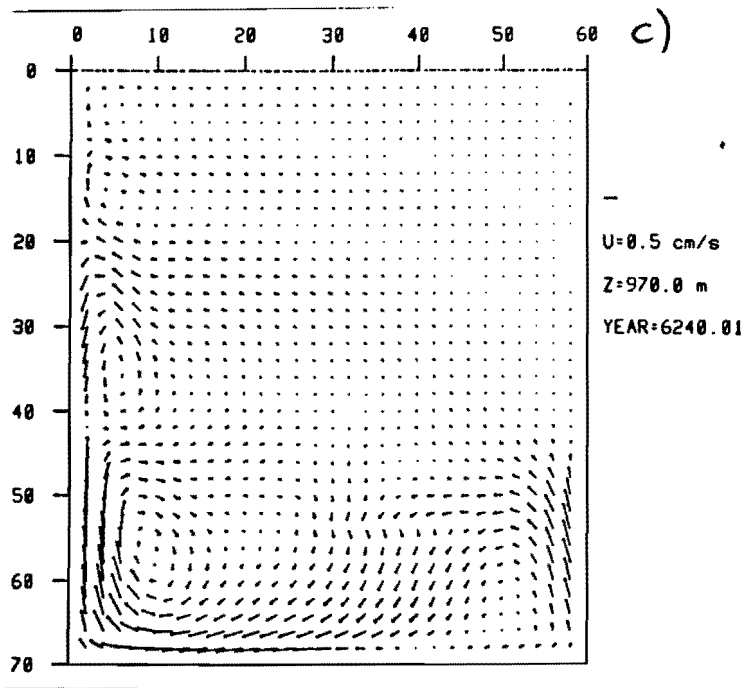
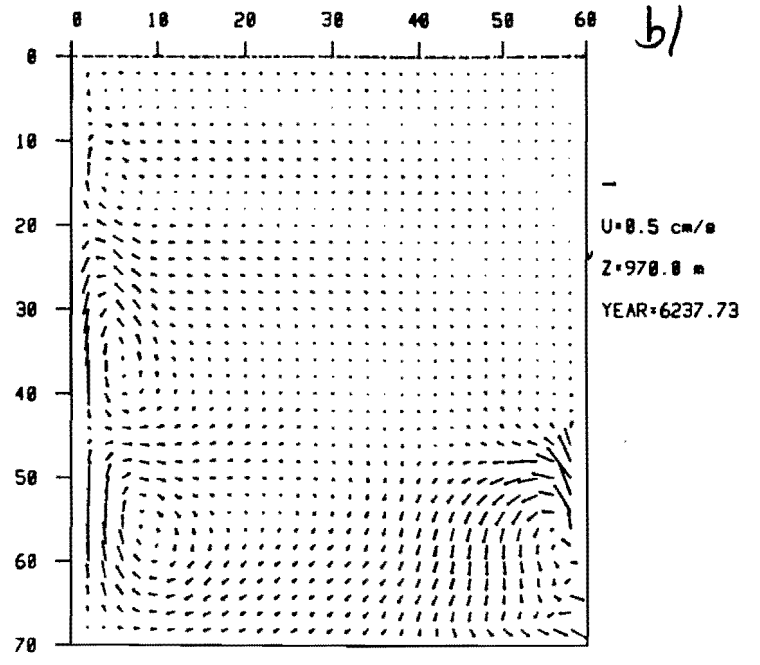
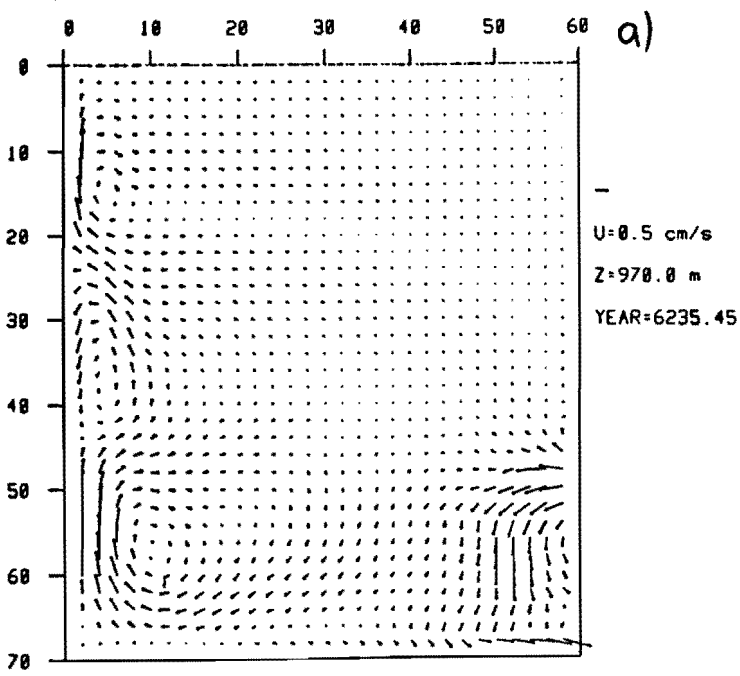


Fig. 13

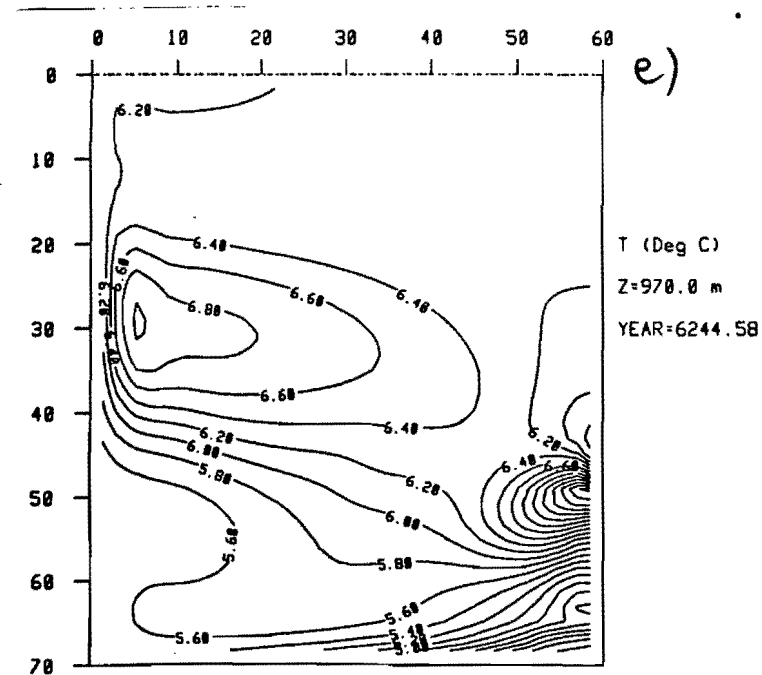
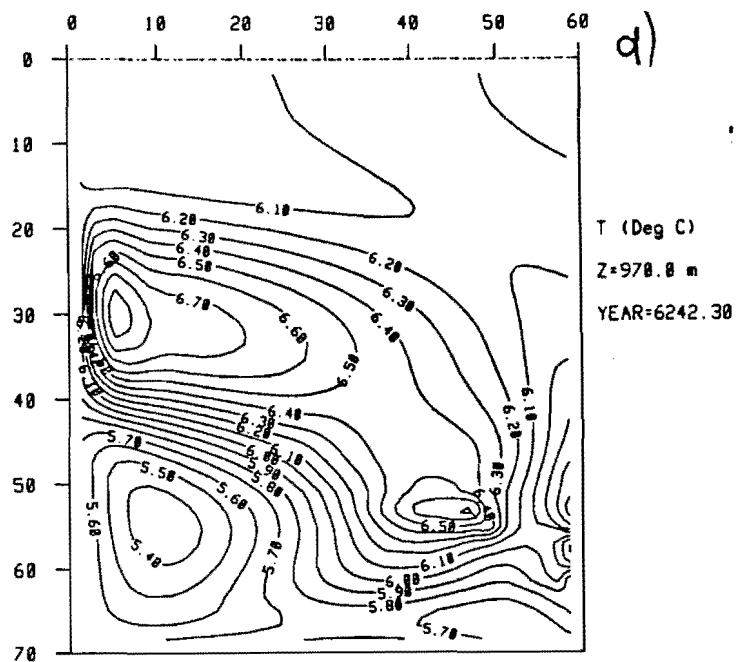
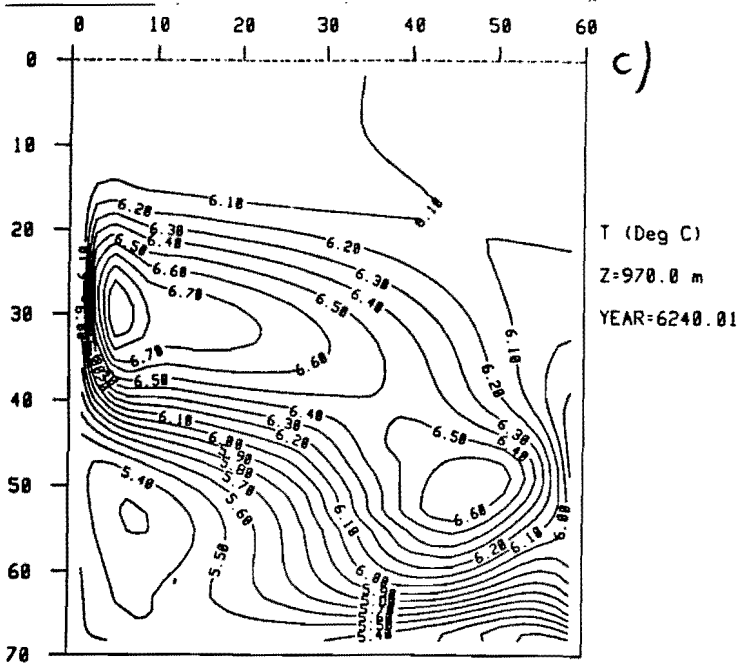
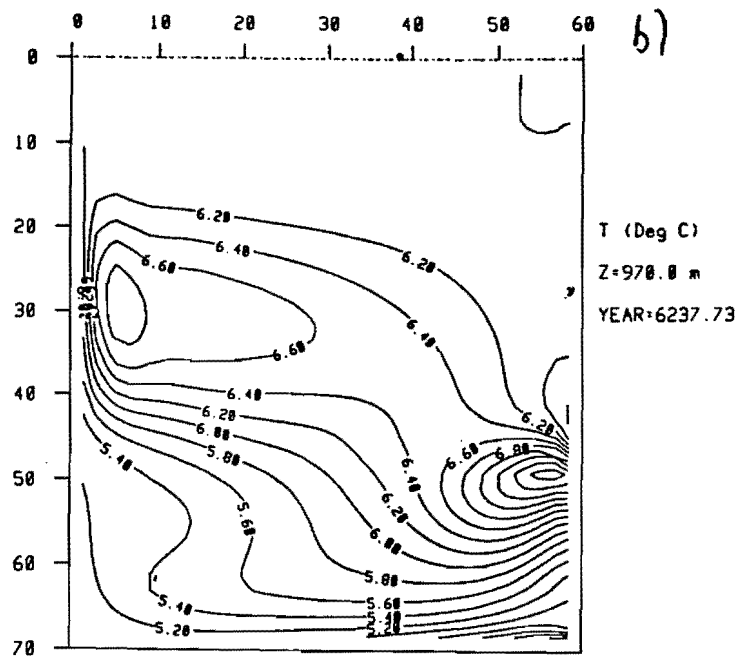
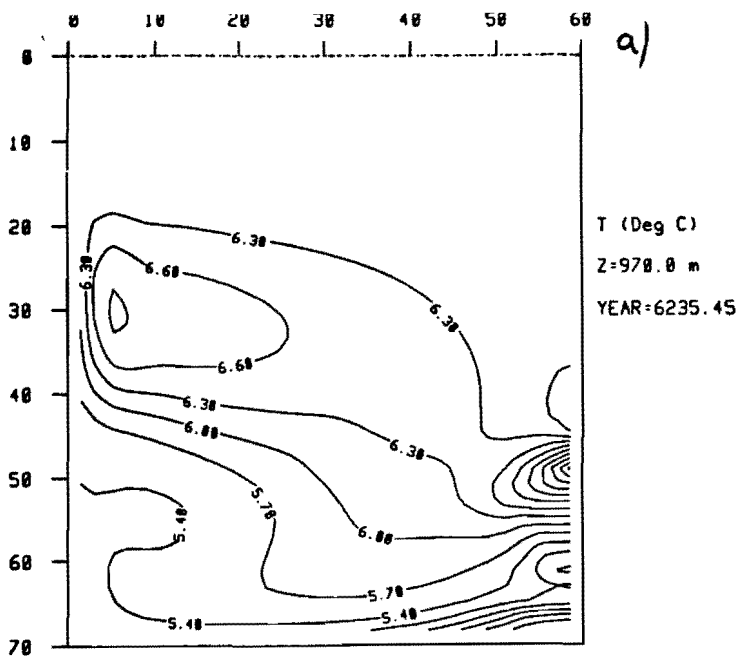


Fig.14.

Poleward Heat Transport Through Oscillation

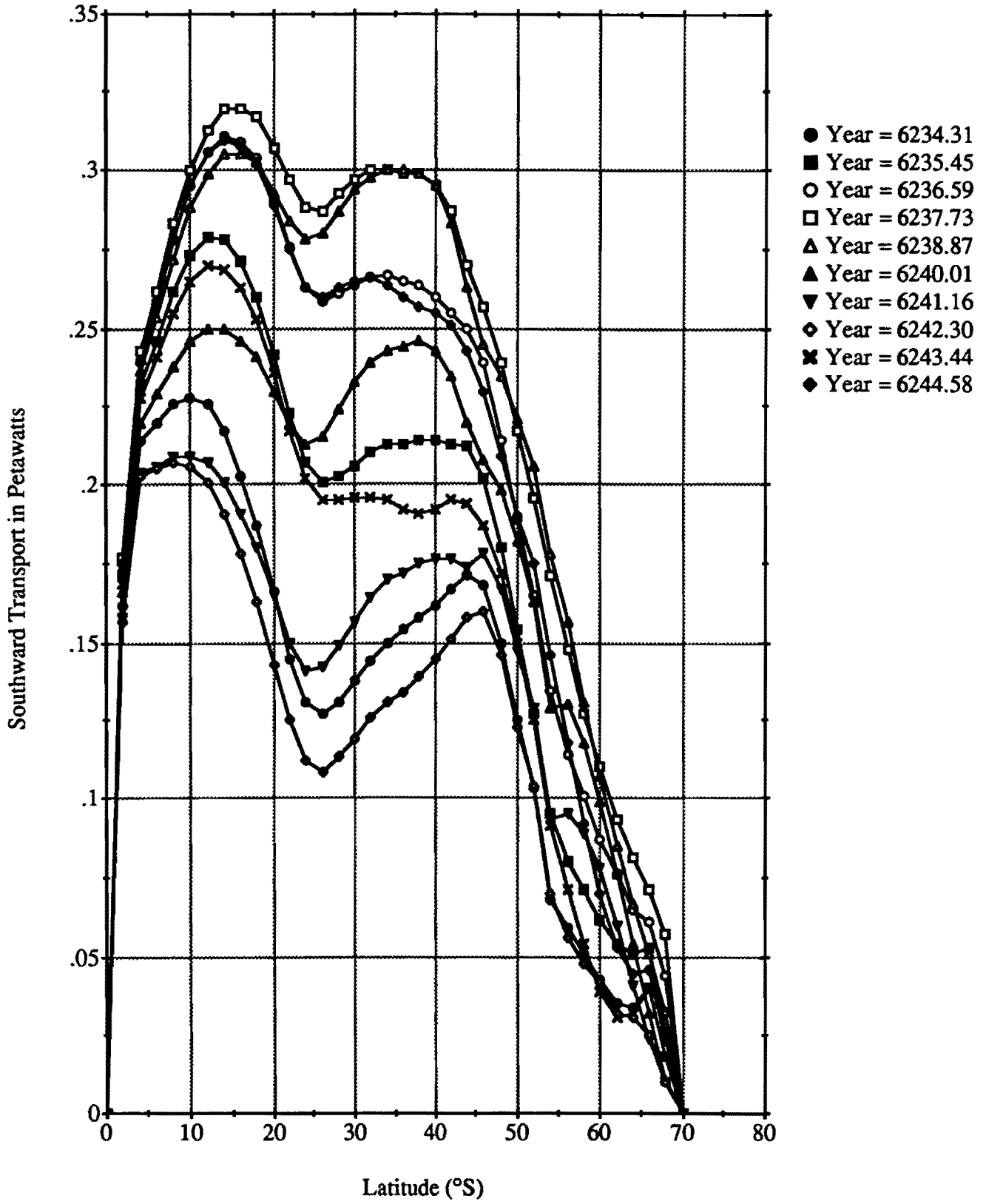


Fig. 15

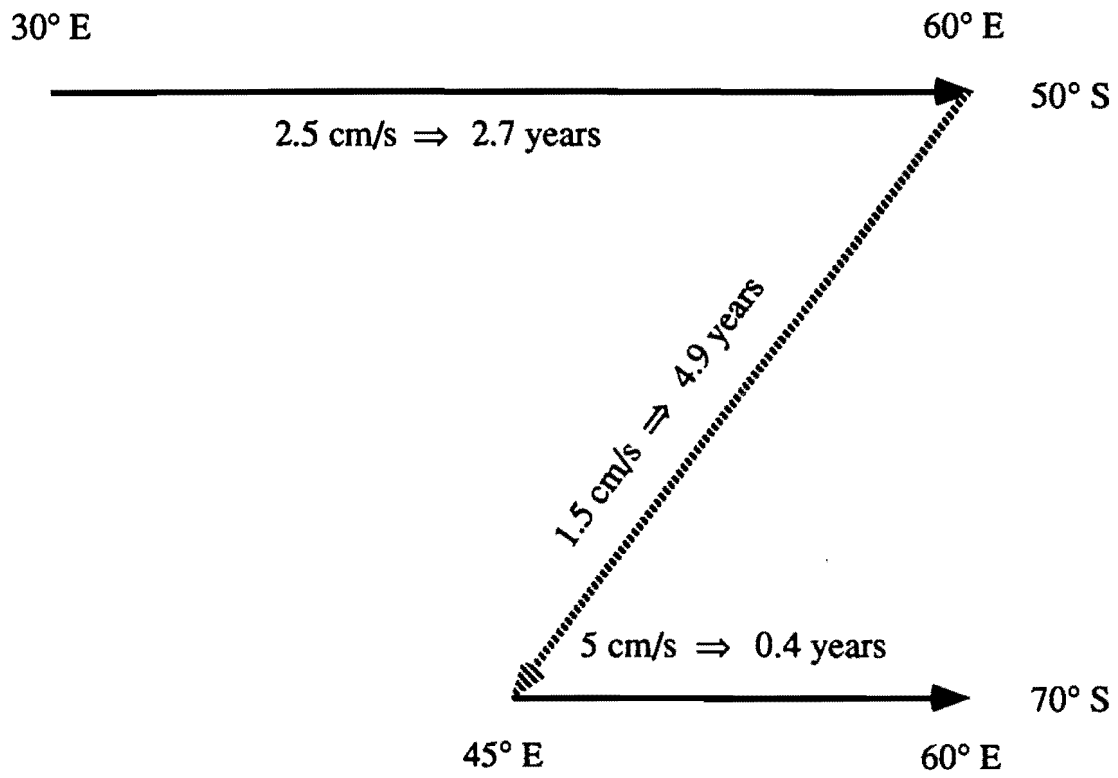


Fig.16.

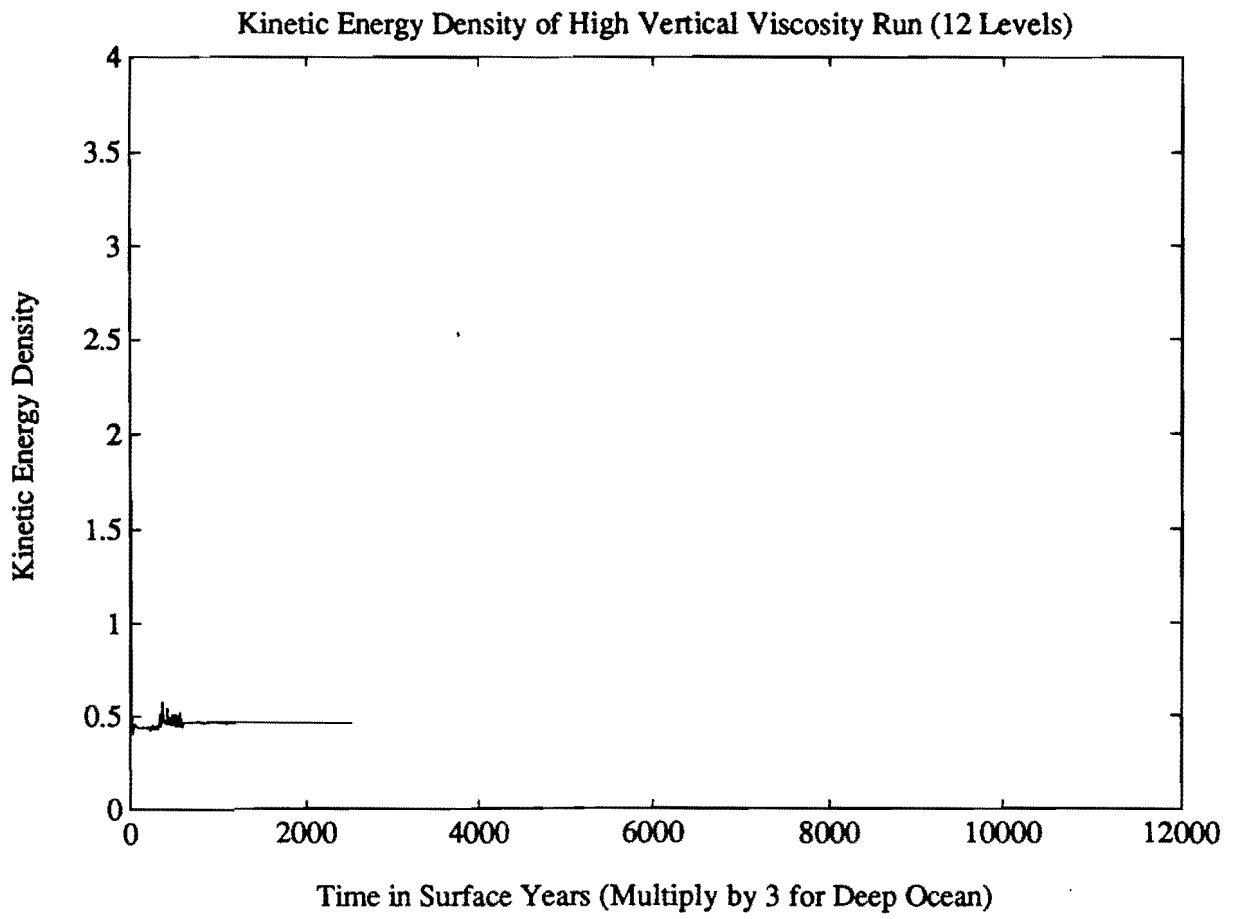


Fig. 1